NATIONAL ADVISORY COMMITTEE FOR AERONAUTICS

TECHNICAL NOTE 3980

INVESTIGATION OF SEMIVANELESS TURBINE STATOR DESIGNED TO PRODUCE AXIALLY SYMMETRICAL FREE-VORTEX FLOW

By Harold E. Rohlik and William T. Wintucky

Lewis Flight Propulsion Laboratory
Cleveland, Ohio

Washington
April 1957

NATIONAL ADVISORY COMMITTEE FOR AERONAUTICS

TECHNICAL NOTE 3980

INVESTIGATION OF SEMIVANELESS TURBINE STATOR DESIGNED TO PRODUCE AXIALLY SYMMETRICAL FREE-VORTEX FLOW

By Harold E. Rohlik and William T. Wintucky

SUMMARY

A semivaneless turbine stator designed to eliminate blade wakes and secondary-flow accumulations of boundary-layer air was built and tested. Performance of this stator was evaluated with static pressures measured in the vaneless section and surveys of total pressure and flow angle made at the stator exit.

The experimental results indicated that the semivaneless stator set up free-vortex flow which was substantially free of circumferential gradients in flow angle and total pressure. Loss in total pressure across this stator was slightly greater than that measured with a conventional stator designed for the same exit flow conditions. Radial distribution of momentum loss indicated that the slight additional loss appeared at the inner wall.

INTRODUCTION

The study of the aerodynamic performance of compressor and turbine blade rows is frequently complicated by the occurrence of irregular flow at the inlet of the blade row being studied, which results from localized losses developed in previous blade rows. Consideration of this problem is particularly important in the study of turbine rotor-blade performance because of the high kinetic-energy level of the approaching fluid. Stationary loss patterns resulting from the turbine stator-blade wakes and loss accumulations present to the rotor blade a flow field of pulsating flow angles and velocities with a frequency determined by the rotor speed and number of blades in the stator row. It is apparent, then, that attainment of an inlet flow field free of circumferential gradients and with a specified radial distribution of velocity-diagram parameters could greatly simplify the determination of rotating-blade-row and blade-element performance by separating out the effects of stationary loss patterns. The effects of these patterns on the rotating-blade-row performance would, of course, still remain to be determined.

A semivaneless turbine stator was designed to produce a free-vortex flow with no circumferential variations in total pressure, static pressure, or flow angle. This stator consists of a conventional blade row with hub and tip radii greater than the specified exit radii and a vaneless annular passage which guides the flow to the exit. A cross section through the axis of the stator assembly is shown in figure 1, illustrating the relative sizes of the components. Air is turned in the blade row to design moment-of-momentum at velocities which are lower than the exit velocities because of the greater radii and the greater annular area. The vaneless part of the stator then accelerates the flow to the exit flow condition by reducing hub and tip radii as well as annular flow area. The vaneless section was designed to produce smooth acceleration on both walls according to a three-dimensional solution of the equilibrium and continuity equations.

This stator was designed to produce a free-vortex flow with hub turning of 66.8°, hub critical velocity ratio of 1.295, and no circumferential gradients. Loss accumulations at the exit of the blade row were to be kept to a minimum by the low level of velocities in turning, wherein the kinetic-energy level would be quite low compared with the stator-exit condition. The loss accumulations and wakes were then to be mixed by the vaneless transition section, which elevates the kinetic-energy level by 85 percent while eliminating circumferential gradients associated with the stator blades.

The purpose of this report is to present the design of the semivaneless stator, theoretical and experimental velocities within the vaneless transition section, and results of detailed surveys of pressure and flow angle at the stator exit made with the stator operating at design conditions. Results of the exit surveys are compared with similar information obtained with a more conventional stator designed for the same exit flow conditions.

SYMBOLS

A	area, sq ft
a	parameter, $\dfrac{\cos^2\beta}{r_c} - \dfrac{\sin^2\beta}{r \cos \alpha}$
b	parameter, $\sin \beta \tan \alpha \, (dV_u/dm)$
g	acceleration due to gravity, 32.2 ft/sec^2
K	vortex constant, sq ft/sec
m	distance along streamline in meridional plane, ft

n distance along orthogonal in meridional plane measured from inner wall, ft

p pressure, lb/sq ft

R gas constant, ft-lb/(lb)(°R)

r radius about axis of rotation, ft

r_c radius of streamline curvature in meridional plane, ft

T temperature, °R

V velocity, ft/sec

V_{cr} critical velocity, $\sqrt{\frac{2\gamma gRT'}{\gamma + 1}}$

w weight flow, lb/sec

α angle between streamline in meridional plane and axis of rotation, deg

β angle between velocity and component of velocity along streamline in meridional plane, deg

γ ratio of specific heats

θ^* momentum-loss parameter, ratio of momentum thickness to blade spacing normal to flow

ρ density, lb/cu ft

Subscripts:

an annular

h hub

i inner wall

id ideal

o outer wall

t tip

u circumferential direction

x axial direction

0 station in inlet tank

1 station just upstream of stator-blade row (fig. 7)

2 station just downstream of stator-blade row (fig. 7)

3 station at exit of semivaneless stator (fig. 7)

Superscript:

' stagnation condition

STATOR DESIGN

The semivaneless turbine stator was designed for free-vortex flow, hub turning of 66.8°, a hub critical velocity ratio of 1.295, and a 0.6 hub-tip radius ratio. This design point was selected to coincide with that of an existing conventional turbine stator for which performance data were available. Both stators were designed for an inlet equivalent weight flow of 21.17 pounds per second with an assumed loss total-pressure ratio of 0.97. The velocity diagrams are shown in figure 2.

Stator-Blade Design

The blades of this stator are designed to produce free-vortex flow. Air passing through the transition section will then have one value of moment-of-momentum at all points on all streamlines. With the vortex flow condition and equivalent weight flow specified, a number of tip radii and annular areas at the blade exit were considered in selecting a blade-exit design point. Figure 3 shows the effect of variation of these parameters on blade-exit hub conditions for a blade-row loss total-pressure ratio of 0.98. The parameters are shown in ratio form.

Selection of the design point on figure 3 was somewhat arbitrary and resulted from the following considerations:

(1) Velocities were to be definitely subsonic in order to keep the kinetic energy relatively low in the vicinity of the blades.

(2) Tip diameter was to be near the minimum consistent with the first requirement. Minimizing this dimension also minimizes frontal area and axial length of the transition section for any specified minimum wall curvature in the meridional plane.

(3) Minimum hub diameter was desirable since it would minimize the necessary change in inner-wall radius and, hence, the inner-wall curvature and/or axial length.

Examination of figure 3 shows that each radius ratio has a minimum critical velocity ratio within or very near the range of area ratios considered. A tip radius ratio of 1.250 was selected because it resulted in a minimum velocity of the desired level. The point chosen on this line of 1.25 tip radius ratio represents a hub radius ratio $r_{h,2}/r_{h,3}$ of 1.542 and was a compromise between considerations of low-velocity level and minimum change in inner-wall radius. The annular area ratio selected is 1.10. Larger ratios result in smaller inner-wall radius changes but would also mean higher inner-wall velocities. Flow angle was included in the analysis simply to ensure a reasonable value. Hub and tip diameters corresponding to the design point selected are 14.8 and 20.0 inches, respectively, with corresponding stator-exit diameters of 9.6 and 16.0 inches.

4356

The hub, mean, and tip blade-exit velocity diagrams resulting from this choice of diameters, the required weight flow, and the free-vortex flow distribution are shown in figure 4. These velocity diagrams provide design moment-of-momentum with a kinetic-energy level of 54 percent of the stator-exit kinetic energy.

The number of blades in the stator was set at 30, and the passages were drawn with straight suction surfaces downstream of the throats. Leading- and trailing-edge radii were 0.015 and 0.010 inch, respectively. Blade surface and midchannel velocities were then calculated to satisfy continuity; simple radial equilibrium for midchannel conditions at hub, mean, and tip radii; and the two-dimensional stream-filament channel analysis described in appendix A of reference 1 at each section. The first trial was considered satisfactory and resulted in blade solidities of 2.1, 1.9, and 1.7 at hub, mean, and tip, respectively. Channel velocities are shown in figure 5 for the hub, mean, and tip sections between the first and last orthogonals calculated. The blade profiles are shown in figure 6, and the coordinates are given in table I.

Transition-Section Design

The design of the vaneless transition section involved a three-dimensional solution for continuity, free-vortex conditions, and equilibrium. Axial symmetry in the flow throughout the transition section was assumed in calculating velocity distributions; so the inner and outer walls were laid out in the meridional plane (plane passing through the axis of rotation) to determine geometrical parameters for the flow equations.

A brief statement of the velocity calculation for each orthogonal in the meridional plane is as follows:

(1) Measurements of α and r_c were made at the end walls and three approximate streamlines in the meridional plane.

(2) The circumferential component of velocity V_u was then calculated at intervals of $n_o/4$ along the orthogonal as a function of r according to the following equation: 4356

$$V_u = \frac{K}{r} \tag{1}$$

where K is the vortex constant specified at the stator exit.

(3) Values of β were then assumed at the inner wall and a distance of $n_o/4$ from the inner wall.

(4) Knowledge of β and V_u at the inner wall specified the corresponding V since

$$V = \frac{V_u}{\sin \beta} \tag{2}$$

(5) The following equation from reference 2 was then used to calculate V at a distance of $n_o/4$ from the inner wall:

$$V = e^{\int_0^n a\, dn}\left(V_i - \int_0^n be^{-\int_0^n a\, dn}\right) dn \tag{3}$$

where

$$a = \frac{\cos^2\beta}{r_c} - \frac{\sin^2\beta}{r \cos \alpha} \tag{3a}$$

$$b = \sin \beta \tan \alpha \, (dV_u/dm) \tag{3b}$$

Equations (3a) and (3b) are presented here in a simplified form corresponding to no rotation of the blade row.

The calculated value of V at a distance of $n_o/4$ from the inner wall with the value of V_u specified by equation (1) at this point gave a new value of β to compare with the assumed value. This permitted a trial-and-error solution for β and V.

This procedure was repeated at intervals of $n_o/4$ until the outer wall was reached. The result was flow distribution along the orthogonal consistent with the assumed value of β at the inner wall, the specified geometry, and the vortex distribution of the tangential component of velocity. The resulting velocity and angle distributions were then used to check continuity with the following equation:

$$w = 2\pi \rho' V_{cr} \int_0^{n_o} \frac{\rho V}{\rho' V_{cr}} \cos \beta \, r \, dn \tag{4}$$

4356

The calculations of continuity through this stator were for standard sea-level conditions at the stator inlet with a 2-percent drop in total pressure in the blade row, as stated previously, and an additional 1-percent through the transition section. A linear variation in total pressure with axial distance through the transition section was used.

Exploratory calculations with the walls contoured approximately in sine waves indicated that the most critical part of the transition section is near the exit, where the flow is approaching the exit flow condition. Here the wall and streamline curvature in the meridional plane is opposite in sign to the curvature about the axis of rotation. This causes the velocity gradient along an orthogonal to be smaller than that which exists in the exit cylindrical annulus where design flow distribution exists. The circumferential component of velocity is a function of radius only; so this reduction in the velocity gradient results in lower through-flow velocities near the inner wall. This means that a tendency toward overturning near the inner wall and underturning near the outer wall will exist with a corresponding streamline shift away from the inner wall. The part of the transition section near the inlet, however, has curvature which is additive with the curvature about the axis. This, then, results in a streamline shift toward the inner wall with the flow turning toward the axial direction, while at the outer wall the flow is turned away from the axial direction. In one of the early trials, values of r_c near the exit were relatively low, setting up a velocity gradient which led to greatly excessive mass flows for all reasonable values of β at the hub. It became apparent that this geometry at design weight flow would lead to a mass-flow void near the exit at the inner wall with a value of β of 90° near the first streamline. No difficulty was experienced near the inlet of the transition section because of the greater radii and the hub-tip radius ratio which specified a much smaller change in V_u along the orthogonal.

Subsequent trials in establishing a design geometry were devoted largely to increasing the radius of curvature of the walls near the exit of the stator and, consequently, increasing the axial length of the transition section. The resulting wall profiles are shown in figure 7 and the coordinates are given in table II.

Calculations of velocities with the final geometry were made along six orthogonals with an assumed streamline pattern. The resulting velocities and flow angles were then used to calculate a new streamline pattern.

A second solution for velocity and angle distributions using the new streamline geometry resulted in little change in velocities at the walls. Velocities calculated in both trials were considered satisfactory throughout the transition section, however; so no additional trials were made, and the solution was considered adequate. 4356

Figure 8 shows the distribution of critical velocity ratio in the transition section resulting from the second trial. This figure shows fairly smooth acceleration everywhere except in two small areas near the outer wall where some deceleration occurs.

Figure 9 shows the distribution of β corresponding to the velocity distribution of figure 8. This figure clearly shows the effect of wall and streamline curvature. Near the exit a large gradient in angle across the passage exists with very high turning near the inner wall and relatively low turning at the outer wall. Near the inlet, where the meridional streamline curvature is opposite in sign from curvature about the axis of rotation, the effect of wall curvature on flow angle was reversed but much less pronounced.

The calculated angle distribution was used to project a radial line at the blade exit, station 2, along streamlines in the transition section to station 3. Figure 10 shows the progressive distortion of this line, which approximates a stator-blade wake, as it moves through the transition section. The projections of five such lines one blade spacing apart are shown in the plane of station 3 to illustrate proximity of adjacent blade wakes after acceleration through the transition section. The smaller helix angles and radii along the inner wall result in a much greater circumferential displacement there than anywhere else, 150° compared with 76° at the mean and 54° at the tip. This figure and consideration of the change in kinetic energy through the transition section indicate the likelihood of considerable mixing of all radii, with the greatest mixing occurring near the inner wall.

APPARATUS

The cold-air test facility used in this investigation consisted of inlet piping, filter and inlet tanks, test section, discharge collector, and piping to exhaust system. Dry air, passing through a thin-plate orifice in the inlet piping, was used in the investigation.

The 30 steel stator blades were bolted to a steel inner ring with the tips of the blades held between spacers fastened to the outer ring. This arrangement permitted adjustment of the blade settings to ensure proper weight flow. The trailing edges of the stator blades were located about 0.50 inch axially upstream of the beginning of curvature of the transition section. The inner wall of the transition section was made of Fiberglas and the outer wall was machined from a steel weldment, both to the coordinates shown in table II. A photograph of the stator is shown in figure 11.

INSTRUMENTATION

The airflow measurements were made with a standard submerged thin-plate orifice calibrated in the installation by surveying flow through a nozzle at several flow conditions.

Inlet total temperature was measured in the inlet tank about 5 feet upstream of the test section. Inlet static pressures were measured with two taps on the inner wall and two on the outer wall just upstream of the blades (station 1, fig. 7). These pressures were used in the calculation of the inlet total pressure. Eight inner-wall static taps in a radial-axial plane were located 0.20, 0.89, 1.64, 2.39, 3.08, 3.89, 4.58, and 5.39 inches downstream of the start of curvature of the transition section. The outer-wall taps in the same plane were located 0.38, 1.14, 1.88, 2.95, 3.70, 4.38, and 5.13 inches downstream of the blade section. These taps were used to determine experimental velocities.

The transition-section-outlet static pressures at station 3 (fig. 7) were measured with four taps 90° apart at each of the inner and outer walls. All pressures were measured with mercury manometers except the pressure difference across the orifice for the inlet weight flow, which was read with an acetylene-tetrabromide manometer.

Detailed surveys of total pressure and flow angle were made at station 3 with a combination total-pressure and angle probe secured in a self-alining actuator. The measuring head of the probe consisted of three side-by-side tubes of 0.030-inch outside diameter and 0.003-inch wall thickness. Photographs of this probe are shown in figure 12. Total-pressure and flow-angle variations obtained by circumferential and radial traverses of the probe were transmitted by a strain-gage pressure transducer to an X-Y recorder. The total pressure was recorded as a difference between the inlet tank total pressure and the total pressure at the probe.

EXPERIMENTAL PROCEDURE

The first tests with the semivaneless stator were made to check inlet equivalent weight flow, and 95.5 percent of design weight flow was obtained at design stator-exit static- to -inlet total-pressure ratio. After resetting the stator blades, the measured weight flow was within 0.1 percent of the design value.

The stator was tested with a nominal inlet total pressure of 40 inches of mercury absolute and a temperature of 80° F. All experimental data were taken at design exit flow conditions, which were approximated by setting the design value of exit static- to inlet total-pressure ratio, as in the weight-flow check. The exit static pressure used was the average of four inner-wall taps spaced 90° apart and four outer-wall taps spaced 90° apart, all in the exit survey plane of station 3 (fig. 7).

Radial traces of total pressure and flow angle were made with the X-Y recorder. Several radial positions were selected from this trace for circumferential traverses. Circumferential traces at these radii were then made over a span of 22.5°, or slightly less than two stator-blade spacings.

EXPERIMENTAL CALCULATIONS

Inlet total pressure was calculated using the following equation and known values of inlet flow area, inlet total temperature, weight flow, and inlet static pressure:

$$\frac{w\sqrt{T_0'}}{p_1 A_{an,1}} = \left[\frac{2\gamma g}{(\gamma - 1)R}\right]^{1/2} \left\{\left[\left(\frac{p'}{p}\right)_1^{\frac{\gamma-1}{\gamma}} - 1\right] + \left[\left(\frac{p'}{p}\right)_1^{\frac{\gamma-1}{\gamma}} - 1\right]^2\right\}^{1/2} \tag{5}$$

Experimental values of velocities in the vaneless transition section were obtained with wall static-pressure measurements and assumed values of total pressure. The total-pressure variation assumed was the same as that used in the design calculations; a 2-percent total-pressure drop across the blade row and an additional 1-percent drop across the transition section, with this loss of 1 percent occurring linearly with axial distance.

Radial distribution of the momentum-loss parameter θ^* was computed using measured values of inlet total pressure, stator-exit static pressure, and stator-exit surveys of total pressure. This parameter is defined by equations (3) and (18(b)) of reference 3 to represent the momentum loss as a ratio of momentum thickness to blade spacing for a conventional stator. These equations were used in the following modified form to compute the values of θ^* for the semivaneless stator. The modified version simply used inlet tank total pressure p_0' for the free-stream or ideal conditions and measured stator-exit total pressure for the actual parameters:

$$\theta^* = \left(1 - \frac{V}{V_{id}}\right)\frac{\rho V}{\rho_{id}V_{id}} \tag{6}$$

where

$$\frac{V}{V_{id}} = \sqrt{\frac{1 - \left(\frac{p}{p'}\right)_3^{\frac{\gamma-1}{\gamma}}}{1 - \left(\frac{p_3}{p_0'}\right)^{\frac{\gamma-1}{\gamma}}}} \tag{6a}$$

and

$$\frac{\rho}{\rho_{id}} = \left(\frac{p_3'}{p_0'}\right)^{\frac{\gamma-1}{\gamma}} \tag{6b}$$

The radial distribution of θ^* was used to get a single mass-averaged value which, in turn, was used to compute an experimental stator loss total-pressure ratio. The method for obtaining this ratio is described in reference 4.

RESULTS AND DISCUSSION

Experimental Velocities

Experimental values of velocities in the vaneless transition section are shown in figure 13 and are compared with the theoretical distribution. Inner-wall experimental values agree very well with the theoretical values, while outer-wall experimental values indicate lower velocities near the inlet of this section and somewhat higher velocities near the exit. The circumferential component of velocity at any point in this section depends only on radius at that point; so these differences affect only the through-flow component of velocity and the flow angle. An experimental variation of flow angle at the walls was obtained by assuming design distribution of the circumferential component of velocity and using the experimental values of total velocity shown in figure 13.

Figure 14 shows a comparison between the resulting experimental angles and the theoretical-angle variation. The experimental patterns of velocity and flow angles are basically the same as the theoretical with differences in magnitude in the regions of greatest wall curvature. The differences that exist are believed to result primarily from the approximate nature of the theoretical calculation. Additional trials with refined streamline geometry and smaller intervals along each orthogonal would probably result in closer agreement between the theoretical and experimental values. Most important, however, is that there is no indication of separation resulting from excessive negative curvature of the walls in the region near the exit. The angle distribution indicates a reasonable through-flow component of velocity at all points on the inner wall rather than the condition which occurred in an early design trial wherein a mass-flow void was indicated by a value of β of 90° some distance from the inner wall.

Total-Pressure Loss

Total-pressure-ratio contours obtained from surveys made at station 3 with the semivaneless stator are shown in figure 15(a). No trace of the stator-blade wakes remained in the central or hub regions. Near the outer wall, however, circumferential variations from the blade wakes persisted clearly in the boundary layer and to a lesser degree in the free stream between a radius of 7.3 inches and the outer-wall boundary layer. The over-all loss total-pressure ratio was 0.973.

Figure 15(b) shows contours of loss total-pressure ratio for a conventional turbine stator designed for the same exit flow conditions as the semivaneless stator. This stator was tested in the same test facility and with the same instrumentation as the semivaneless stator. The contours in figure 15(b) were obtained from annular surveys made in a radial plane which was approximately 3/4 inch downstream of the trailing edge. The wakes are clearly defined with loss accumulations at both hub and tip, which resulted from cross-channel secondary flows in the end-wall boundary layers. The loss total-pressure ratio across this stator was 0.975.

The difference in total-pressure ratios for the two stators indicates that a slight loss in total-pressure ratio was incurred by the semivaneless stator in achieving the degree of uniformity of total-pressure distribution shown in figure 15(a).

Figure 16 shows a comparison of reproductions of total-pressure traces made with the X-Y recorder for both the conventional and semivaneless stators. This figure shows the variations of total pressure with circumferential distance at four radii for each stator. Since the semivaneless stator produced a flow field approaching axial symmetry, the radial trace of total pressure shown in figure 17 adequately represents the total-pressure distribution at the stator exit.

Flow Angle

The radial distribution of flow angle at station 3 is shown in figure 18. The measured flow angles agree almost exactly with the theoretical free-vortex angle distribution in the inner half of the passage and within 5° in all but the wall boundary layers. The total-pressure and flow-angle surveys, then, indicate that the semivaneless stator was reasonably successful in setting up free-vortex flow without the conventional pattern of blade wakes and secondary-flow accumulations of loss material.

4356

Figure 19 shows the radial variation of θ^* for both the conventional and semivaneless stators. The semivaneless stator showed greater momentum loss near the inner wall, with a thicker boundary layer and a loss region extending to a radius of about 5.6 inches. This resulted in an over-all momentum loss approximately 8 percent greater than that of the conventional stator.

The pressure and momentum losses computed for both stators include normal shock losses at the survey probe in the region of supersonic flow near the inner wall, since the pressure measured occurred downstream of the normal shock. No correction to pressure upstream of the shock was attempted with the conventional stator because of the complicated local gradients in total and static pressures. Earlier attempts at correcting probe-shock losses on the basis of wall static pressures and measured total pressures resulted in overcorrections in some areas and subsequent doubt regarding corrections in all. Shock corrections were made with the semivaneless stator, however, because of the lack of circumferential gradients in pressure. The magnitude of the correction in terms of momentum loss is shown in figure 20, where the shaded area represents survey-probe normal-shock loss. This area is approximately 5.5 percent of the total momentum loss represented in figure 19 for the semivaneless stator. The momentum loss shown for the standard stator includes a probe-shock loss of about the same magnitude since the velocity and total-pressure levels are the same.

SUMMARY OF RESULTS

The semivaneless-stator investigation included a velocity-diagram study for the blade exit, a three-dimensional solution of flow in the vaneless section, and experimental determination of flow conditions and loss characteristics. Results of the investigation may be summarized as follows:

The stator design study showed that the most critical part of the vaneless transition section is near the exit, where the flow approaches the exit cylindrical annulus. Wall and streamline curvatures here are opposite in sign from the curvature about the axis of rotation, causing a streamline shift away from the inner wall as a result of angular momentum and equilibrium considerations. This condition necessitated very low curvature in order to avoid separation from the inner wall.

Experimental velocities within the vaneless transition section showed basically the same flow pattern as the design analysis but with somewhat different magnitudes in the regions of maximum outer-wall curvature. This is believed to be the result of the approximate nature of the three-dimensional flow solution which did not go beyond a second trial in approximating streamline geometry or take into account the presence of wall boundary layers. 4356

Total-pressure measurements made at the exit of the semivaneless stator indicate that this stator effectively eliminated blade wakes and loss accumulations resulting from secondary flows. Momentum loss was slightly greater, about 8 percent, than that of a conventional turbine stator tested at the same flow condition, with the increase in loss appearing at the inner wall. Angle measurements made at this location showed very good agreement with the free-vortex design distribution. Wall velocities calculated with measured static pressures at the stator exit also confirmed vortex flow.

Experimentally determined flow angles on the walls of the vaneless section of the stator indicated a finite through-flow component of velocity at all points and, consequently, no separation resulting from momentum considerations.

This stator was reasonably successful in setting up vortex flow while eliminating stator-blade wakes and loss accumulations.

Lewis Flight Propulsion Laboratory
National Advisory Committee for Aeronautics
Cleveland, Ohio, March 4, 1957

REFERENCES

1. Huppert, M. C., and MacGregor, Charles: Comparison Between Predicted and Observed Performance of Gas-Turbine Stator Blade Designed for Free-Vortex Flow. NACA TN 1810, 1949.

2. Stewart, Warner L.: Analytical Investigation of Flow Through a High-Speed Mixed-Flow Turbine. NACA RM E51H06, 1951.

3. Stewart, Warner L.: Analysis of Two-Dimensional Compressible-Flow Loss Characteristics Downstream of Turbomachine Blade Rows in Terms of Basic Boundary-Layer Characteristics. NACA TN 3515, 1955.

4. Stewart, Warner L., Whitney, Warren J., and Wong, Robert Y.: Use of Mean-Section Boundary-Layer Parameters in Predicting Three-Dimensional Turbine Stator Losses. NACA RM E55L12a, 1956.

4356

4356

TABLE I. - SEMIVANELESS STATOR-BLADE COORDINATES

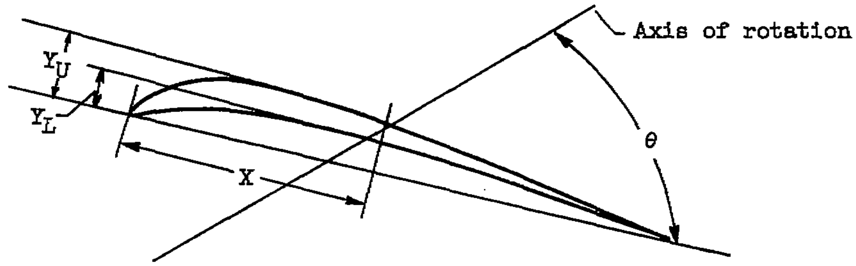

	Hub		Mean		Tip	
	θ					
	53°28'		51°27'		48°24'	
X	Y_U	Y_L	Y_U	Y_L	Y_U	Y_L
0	0.015	0.015	0.015	0.015	0.015	0.015
.1	.160	.060	.139	.052	.153	.048
.2	.246	.121	.221	.104	.239	.092
.3	.302	.168	.277	.143	.296	.126
.4	.342	.205	.316	.172	.336	.150
.5	.370	.235	.344	.196	.363	.170
.6	.388	.256	.362	.213	.379	.185
.7	.399	.272	.374	.226	.389	.196
.8	.404	.284	.379	.234	.393	.203
.9	.405	.291	.380	.241	.393	.208
1.0	.403	.295	.378	.245	.390	.211
1.1	.397	.296	.371	.246	.383	.212
1.2	.388	.294	.362	.246	.373	.212
1.3	.377	.290	.352	.243	.362	.210
1.4	.363	.284	.339	.240	.349	.207
1.5	.347	.276	.325	.234	.335	.203
1.6	.331	.266	.310	.227	.320	.198
1.7	.314	.255	.295	.220	.305	.192
1.8	.297	.244	.280	.211	.290	.185
1.9	.297	.230	.263	.201	.275	.178
2.0	.260	.217	.247	.191	.260	.171
2.1	.241	.202	.231	.171	.245	.164
2.2	.221	.187	.215	.168	.229	.155
2.3	.201	.170	.199	.156	.215	.146
2.4	.182	.154	.183	.144	.198	.137
2.5	.164	.137	.167	.131	.183	.127
2.6	.145	.120	.151	.118	.167	.117
2.7	.126	.101	.134	.104	.151	.106
2.8	.107	.084	.118	.090	.135	.096
2.9	.089	.066	.102	.076	.119	.085
3.0	.069	.048	.087	.061	.103	.072
3.1	.051	.030	.070	.046	.087	.059
3.2	.031	.010	.053	.030	.061	.045
3.262	.010	.010	----	----	----	----
3.3	----	----	.038	.015	.055	.031
3.403	----	----	.010	.010	----	----
3.4	----	----	----	----	.038	.016
3.5	----	----	----	----	.010	.010

TABLE II. - COORDINATES OF WALL CONTOUR BETWEEN

BLADE-EXIT ANNULUS AND STATOR-EXIT ANNULUS

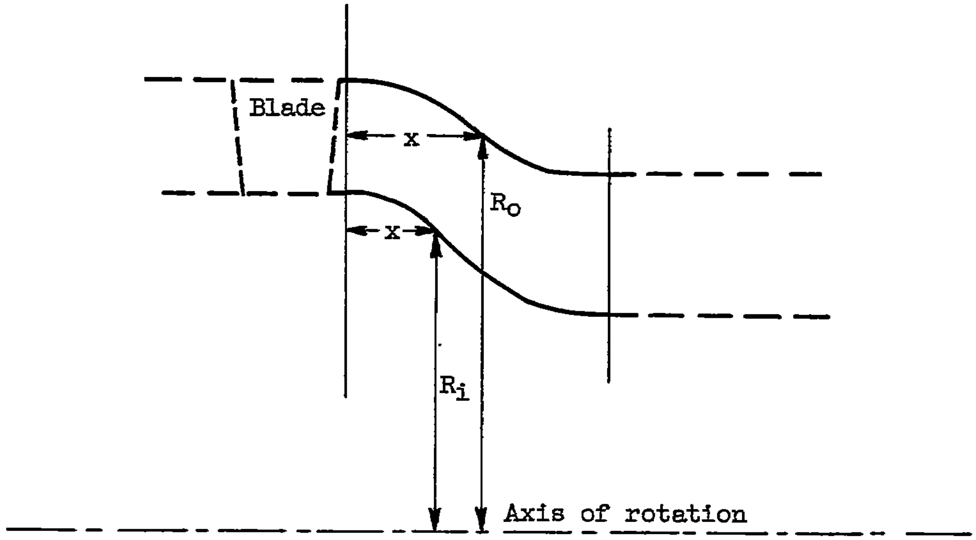

x	R_o	R_i
0.000	10.000	7.400
.200	9.993	7.391
.400	9.980	7.367
.600	9.956	7.323
.800	9.920	7.263
1.000	9.873	7.183
1.200	9.817	7.080
1.400	9.751	6.953
1.600	9.670	6.794
1.800	9.576	6.602
2.000	9.467	6.399
2.200	9.341	6.200
2.400	9.201	6.010
2.600	9.042	5.825
2.800	8.860	5.652
3.000	8.674	5.492
3.200	8.518	5.351
3.400	8.388	5.227
3.600	8.280	5.125
3.800	8.194	5.039
4.000	8.131	4.969
4.200	8.086	4.916
4.400	8.052	4.876
4.600	8.028	4.848
4.800	8.013	4.826
5.000	8.004	4.811
5.200	8.002	4.804
5.400	8.001	4.801
5.500	8.000	4.800

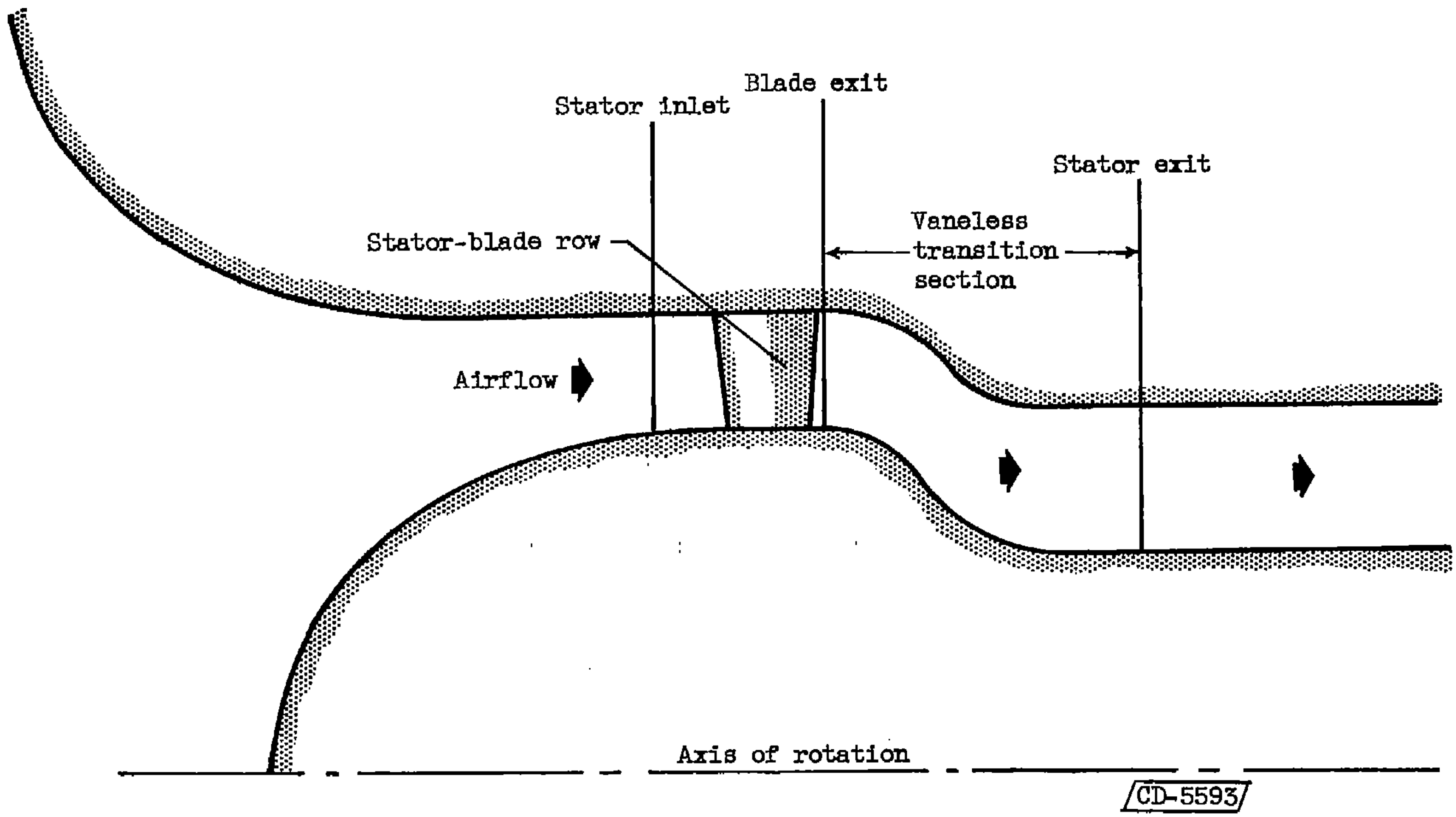

Figure 1. - Cross section of semivaneless turbine stator.

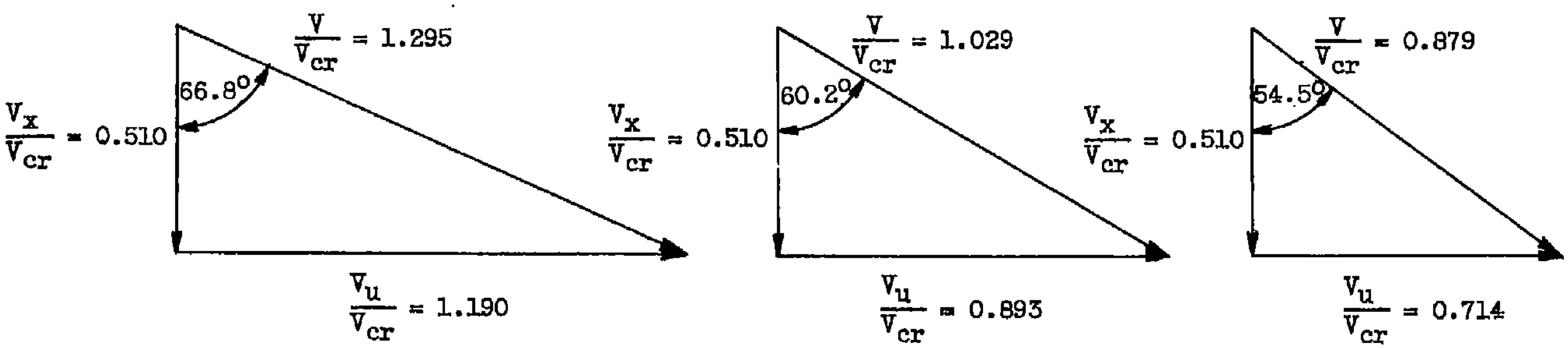

(a) Hub. (b) Mean. (c) Tip.

Figure 2. - Stator-exit velocity diagrams for semivaneless stator (station 3).

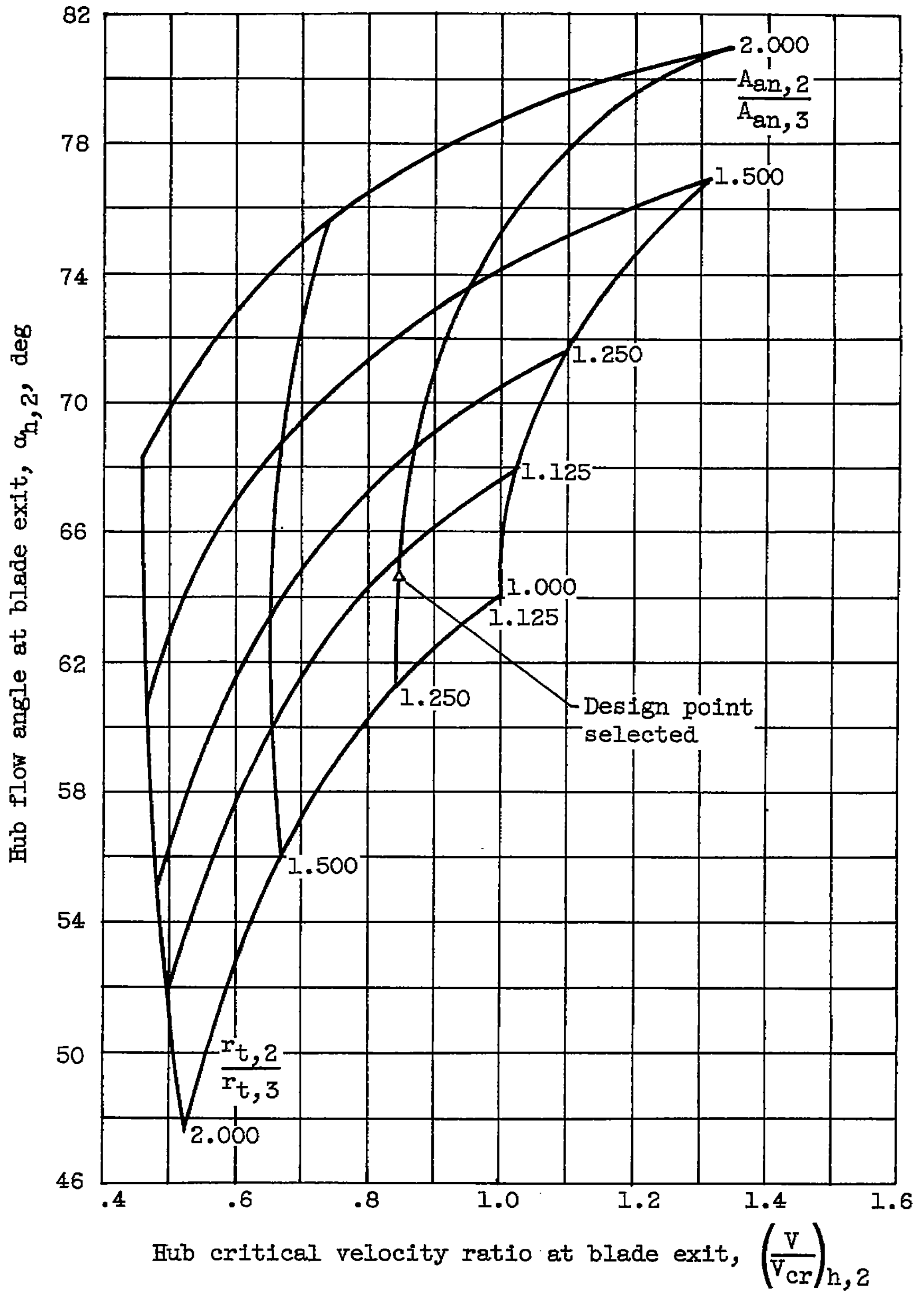

Figure 3. - Hub flow conditions at blade exit for design weight flow, vortex flow distribution, and range of tip-radius and area ratios.

4356

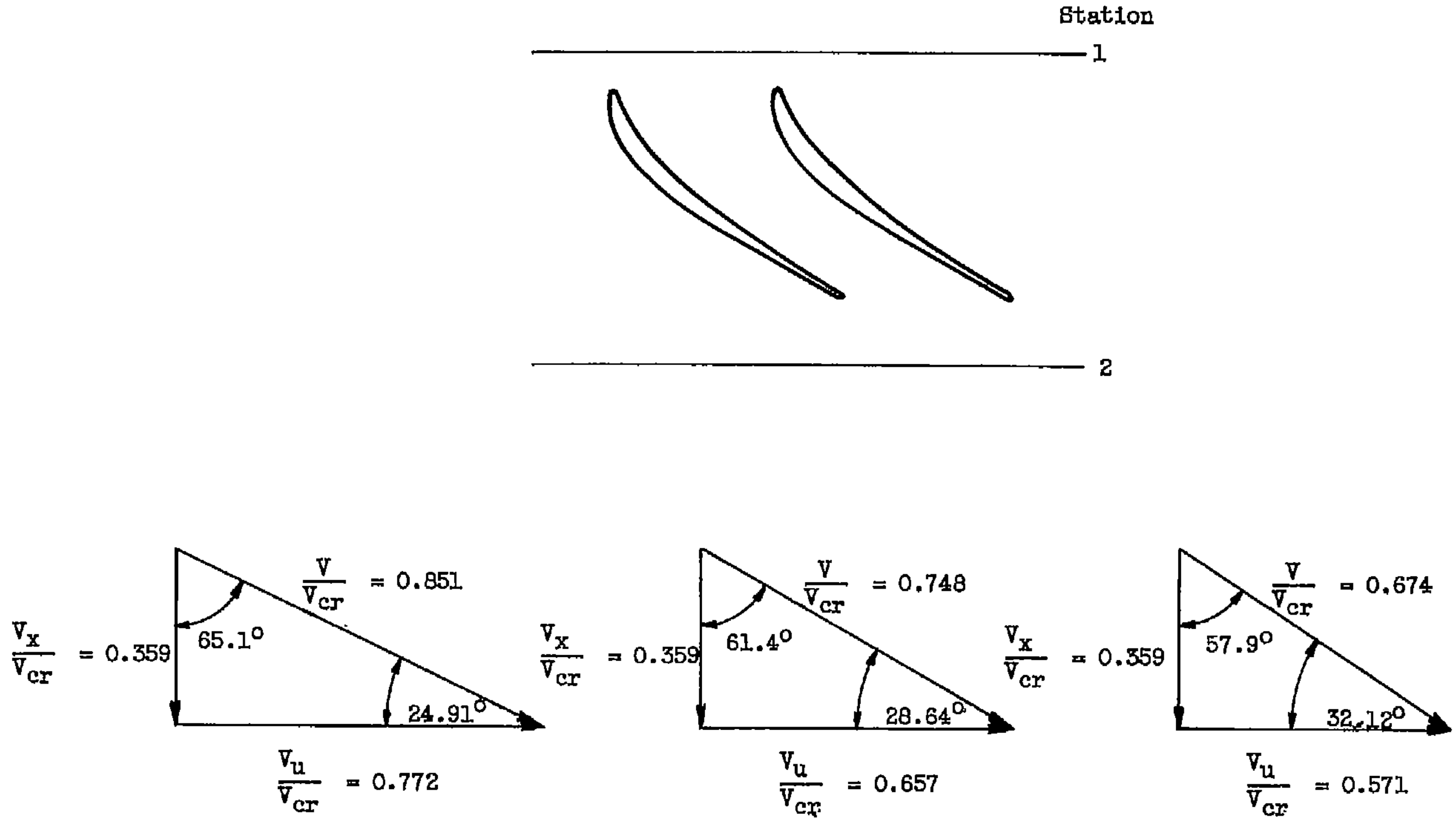

(a) Hub. (b) Mean. (c) Tip.

Figure 4. - Blade-exit velocity diagrams for semivaneless stator (station 2).

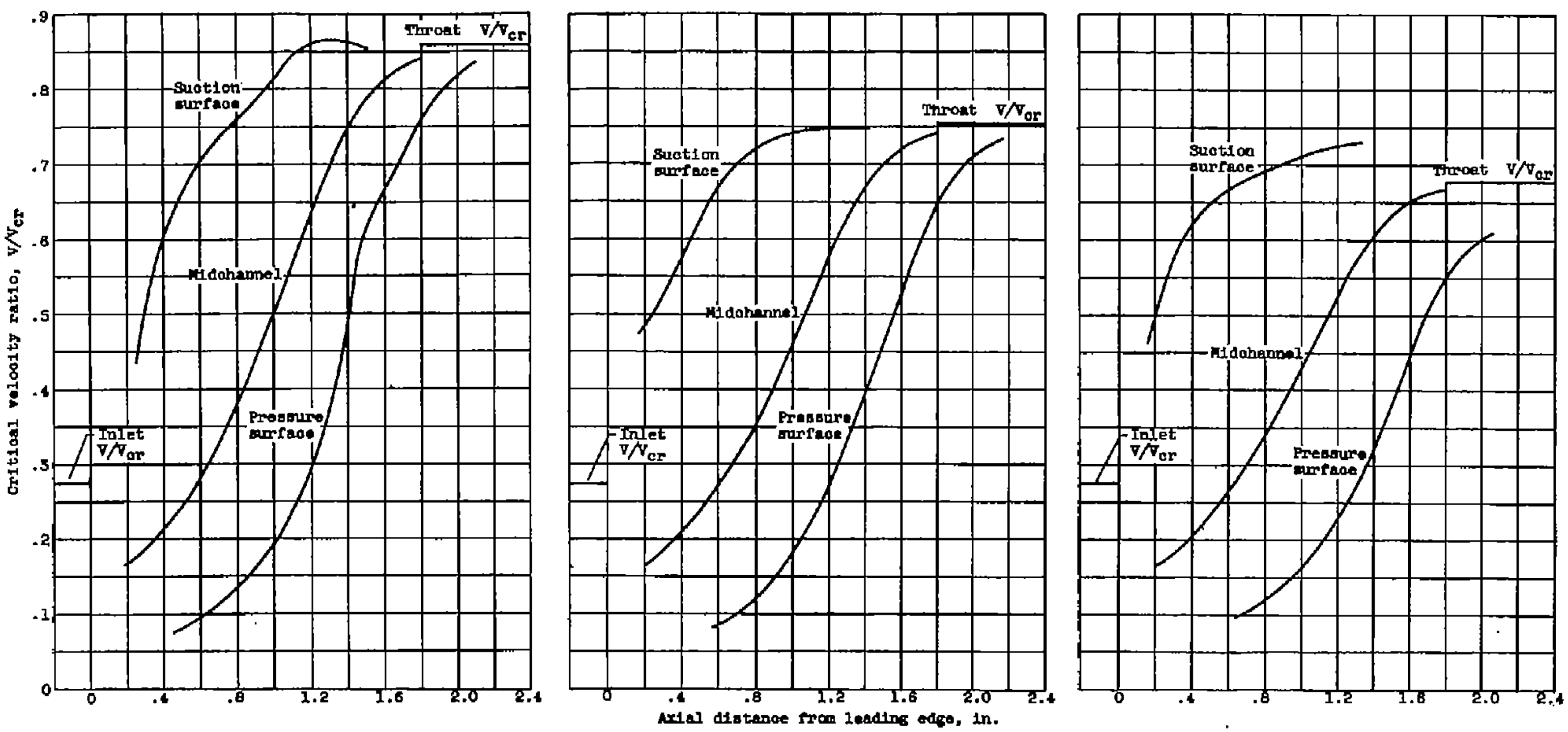

(a) Hub.

(b) Mean.

(c) Tip.

Figure 5. - Surface and midchannel velocity distributions for semivaneless stator.

4356

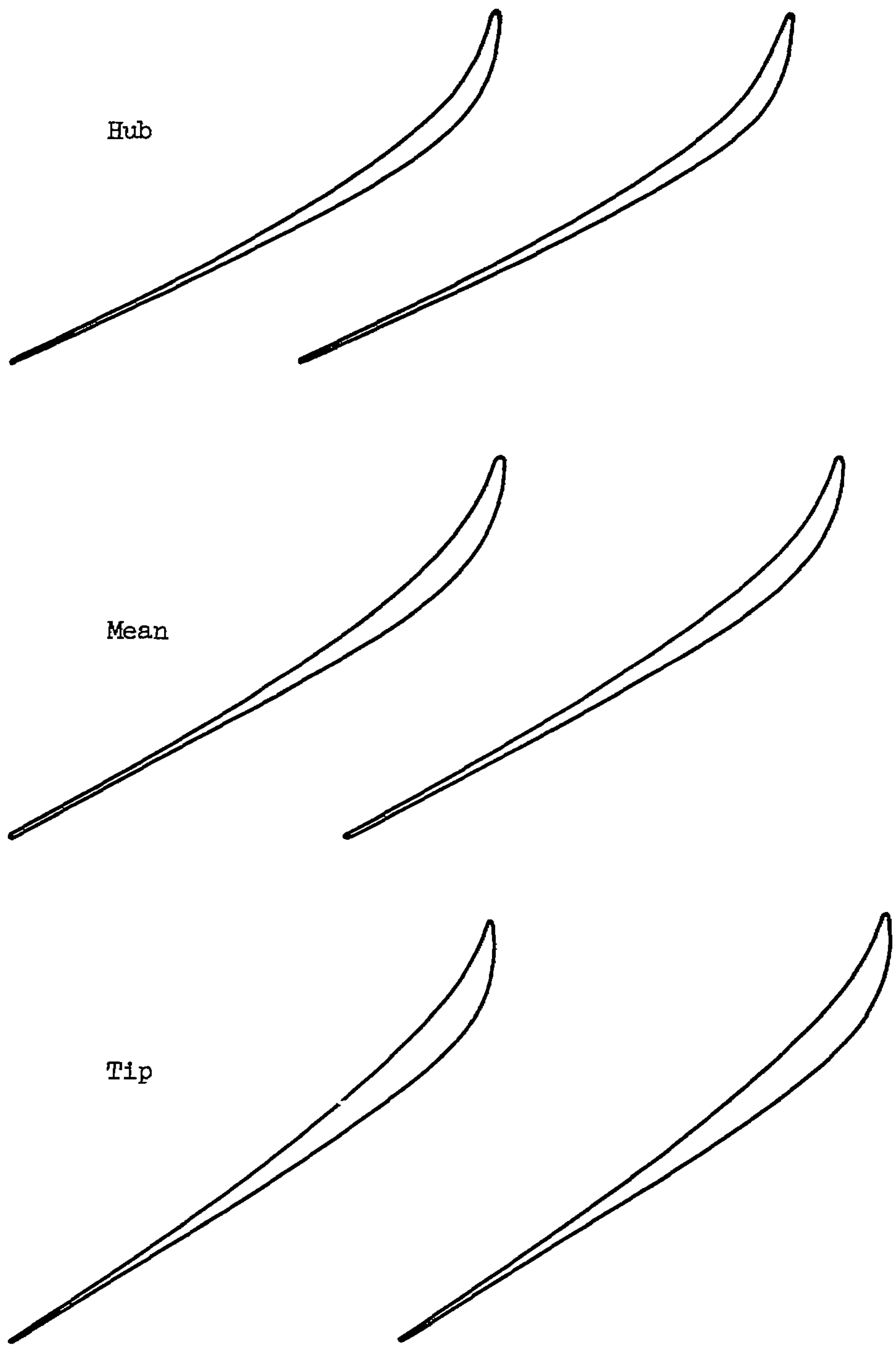

Figure 6. - Stator-blade profiles and passages.

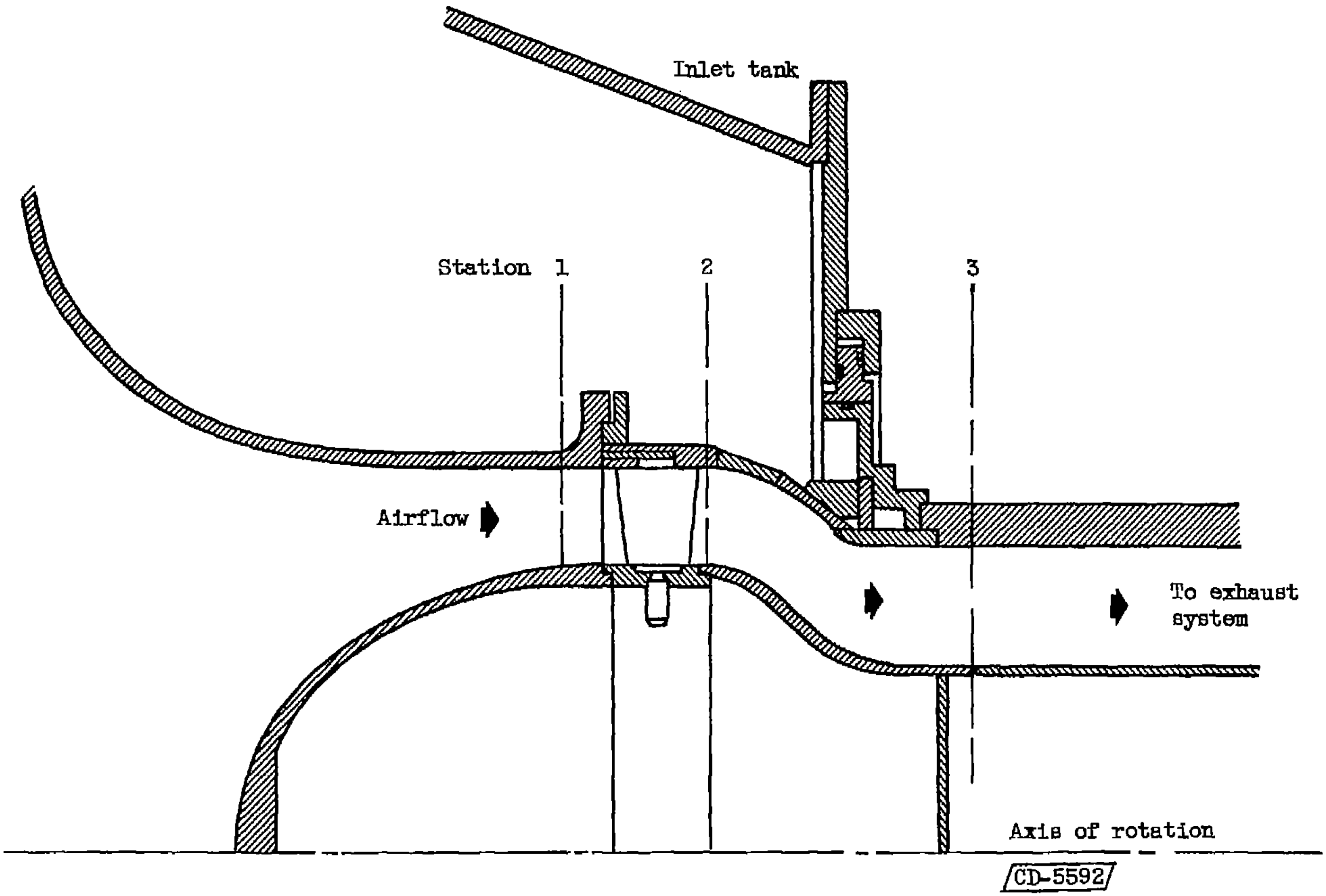

Figure 7. - Diagrammatic sketch of test section used in this investigation.

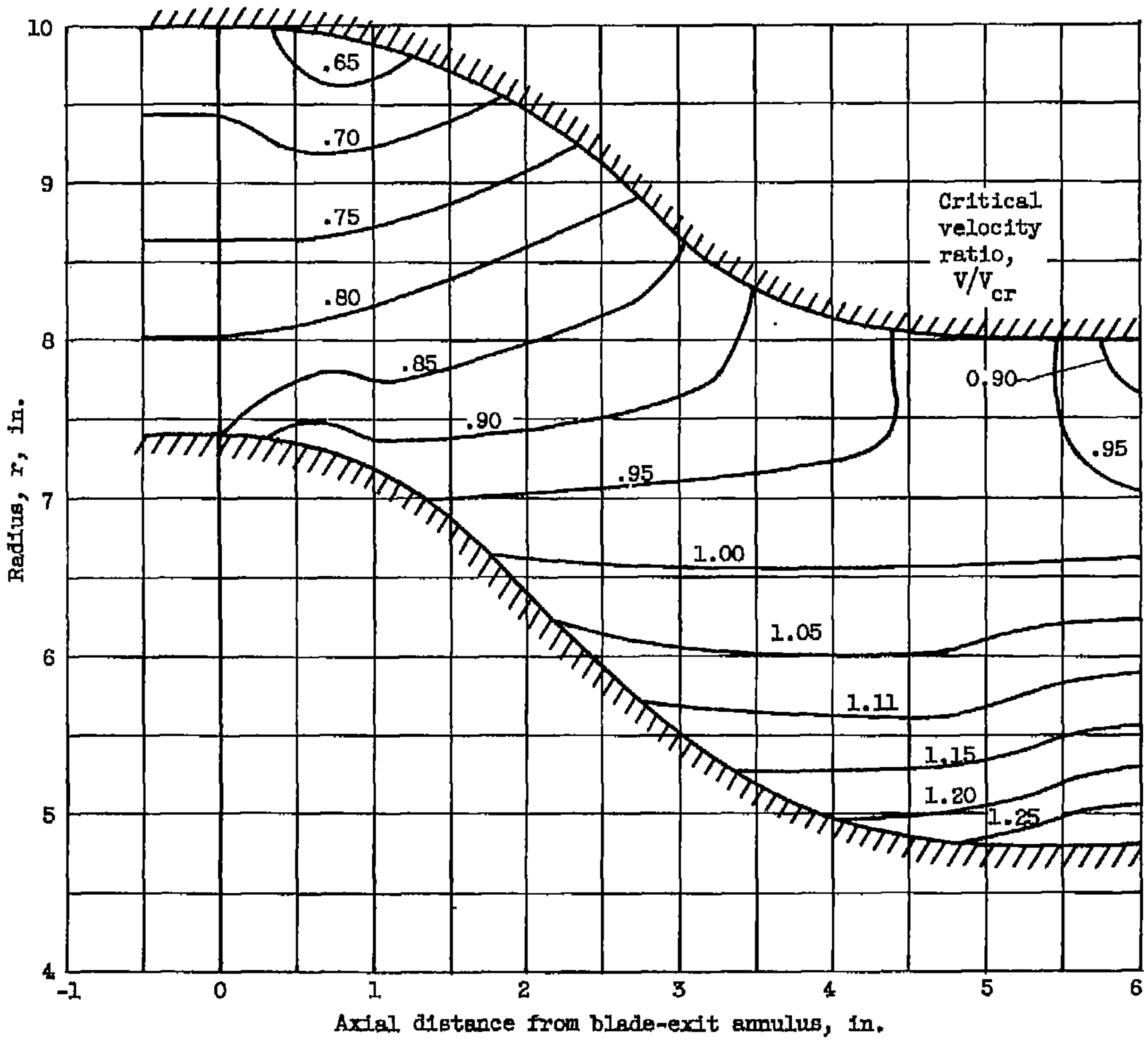

Figure 8. - Contours of calculated critical velocity ratio in transition section.

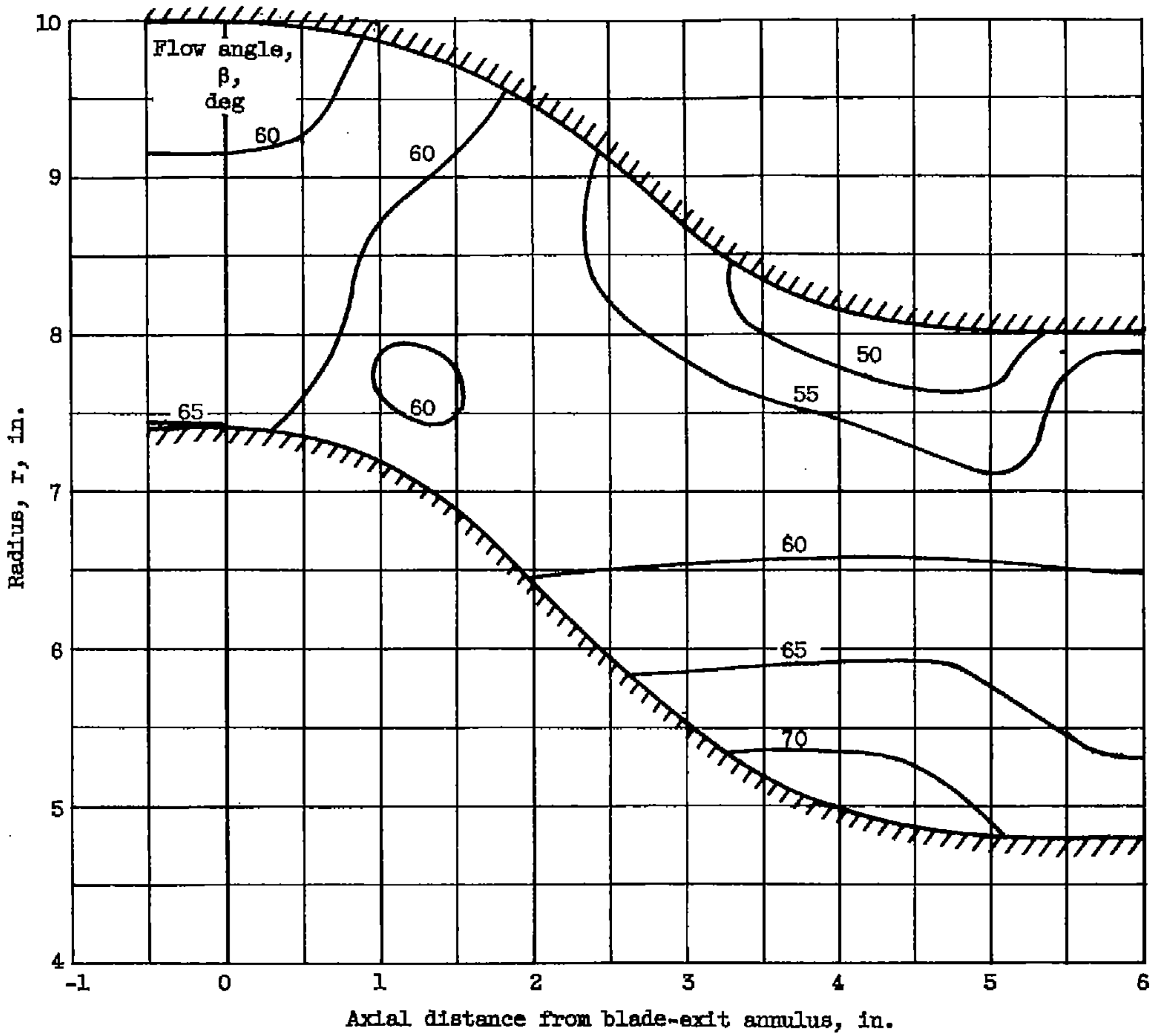

Figure 9. - Contours of calculated flow angle in transition section.

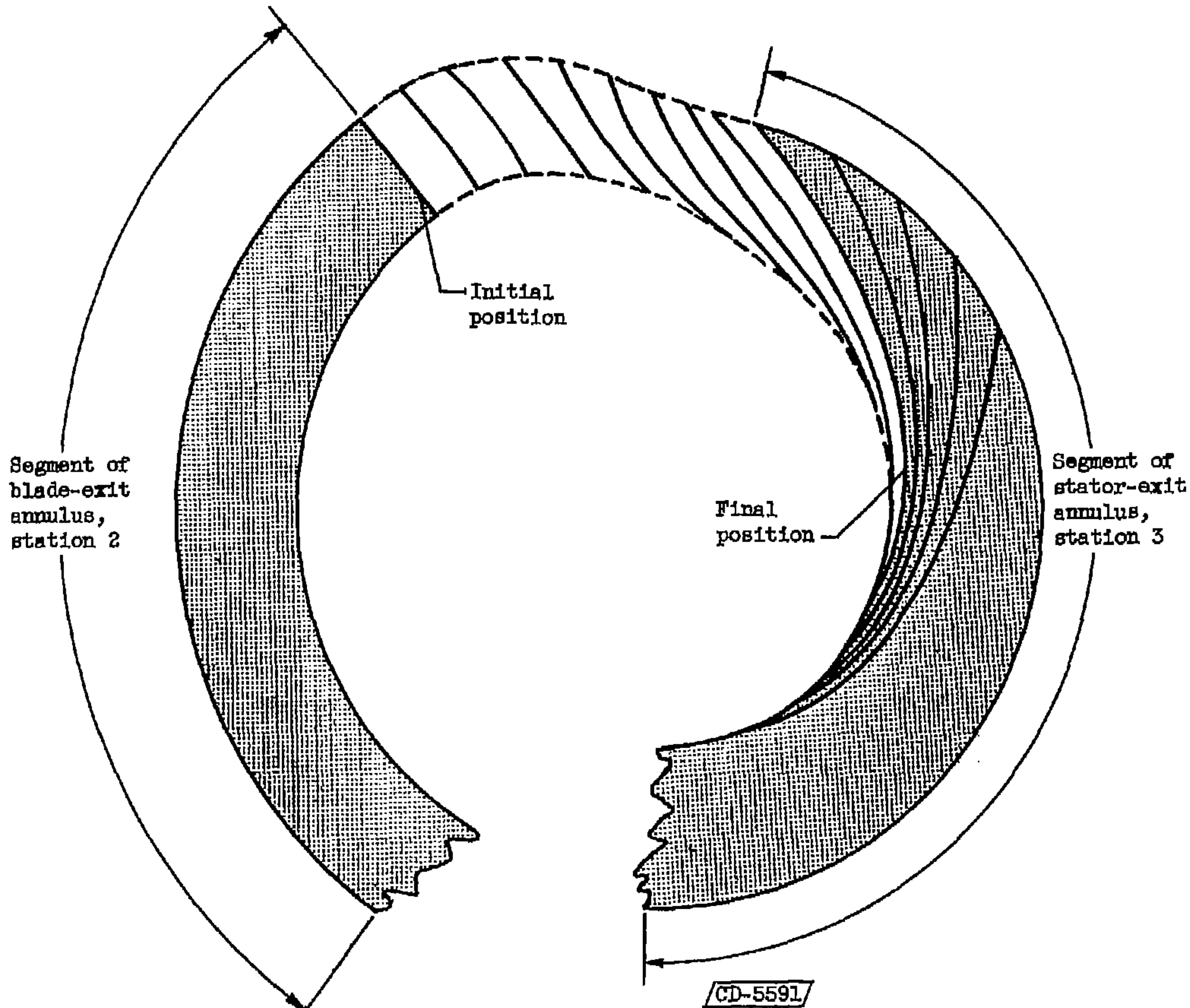

Figure 10. - Axial views of radial line at blade exit projected along streamlines on 10 equally spaced radial planes through transition section to stator exit where five such projections one blade spacing apart are shown.

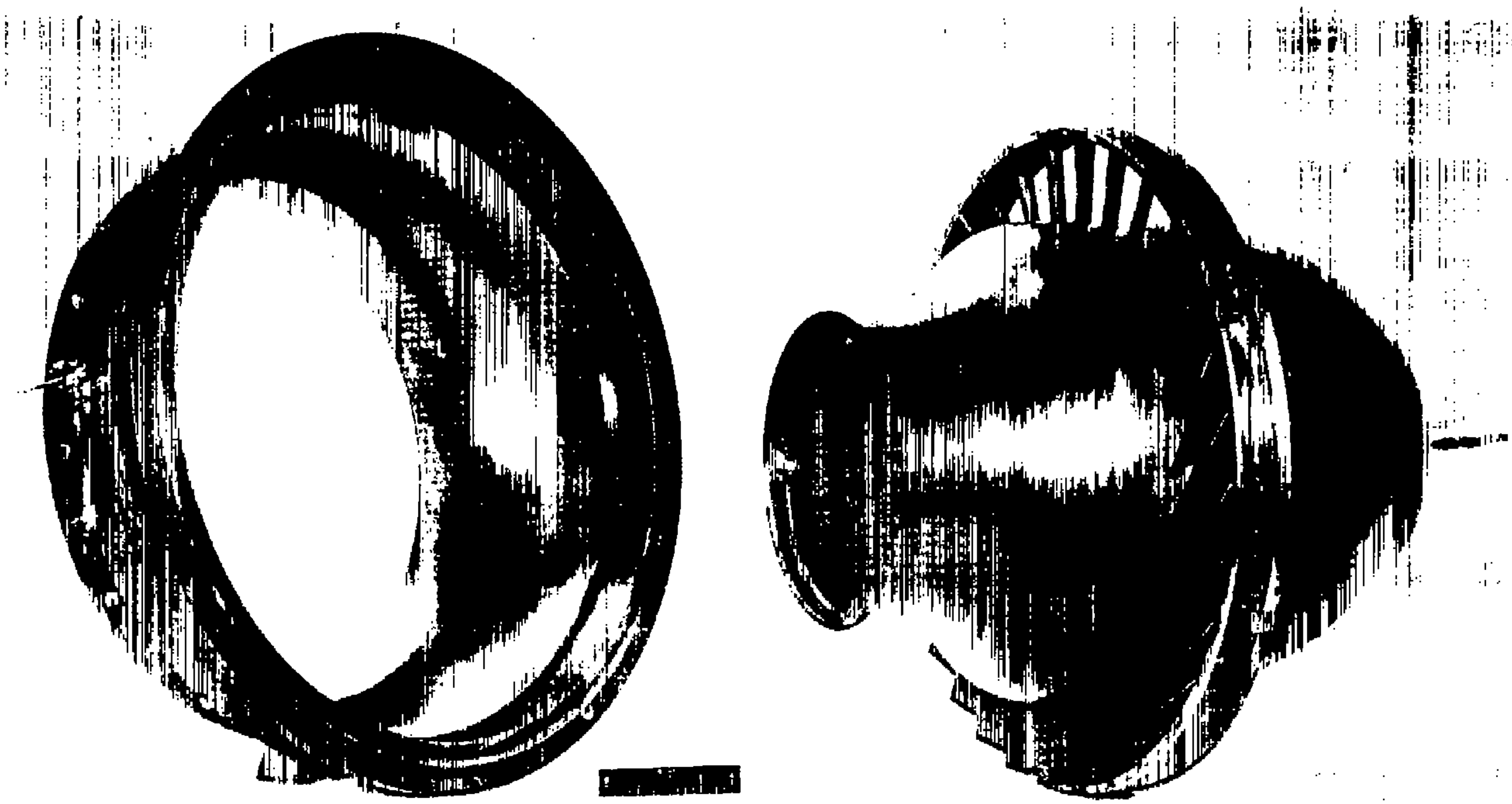

C-43067

Figure 11. - Semivaneless stator.

4356

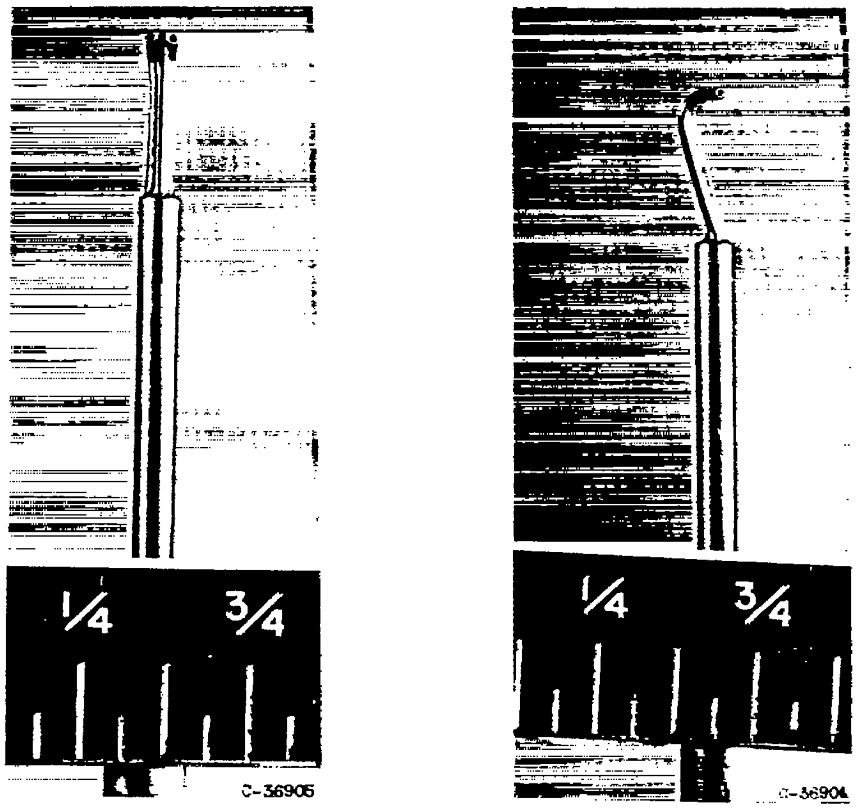

Figure 12. - Probe for measuring total pressure and angle.

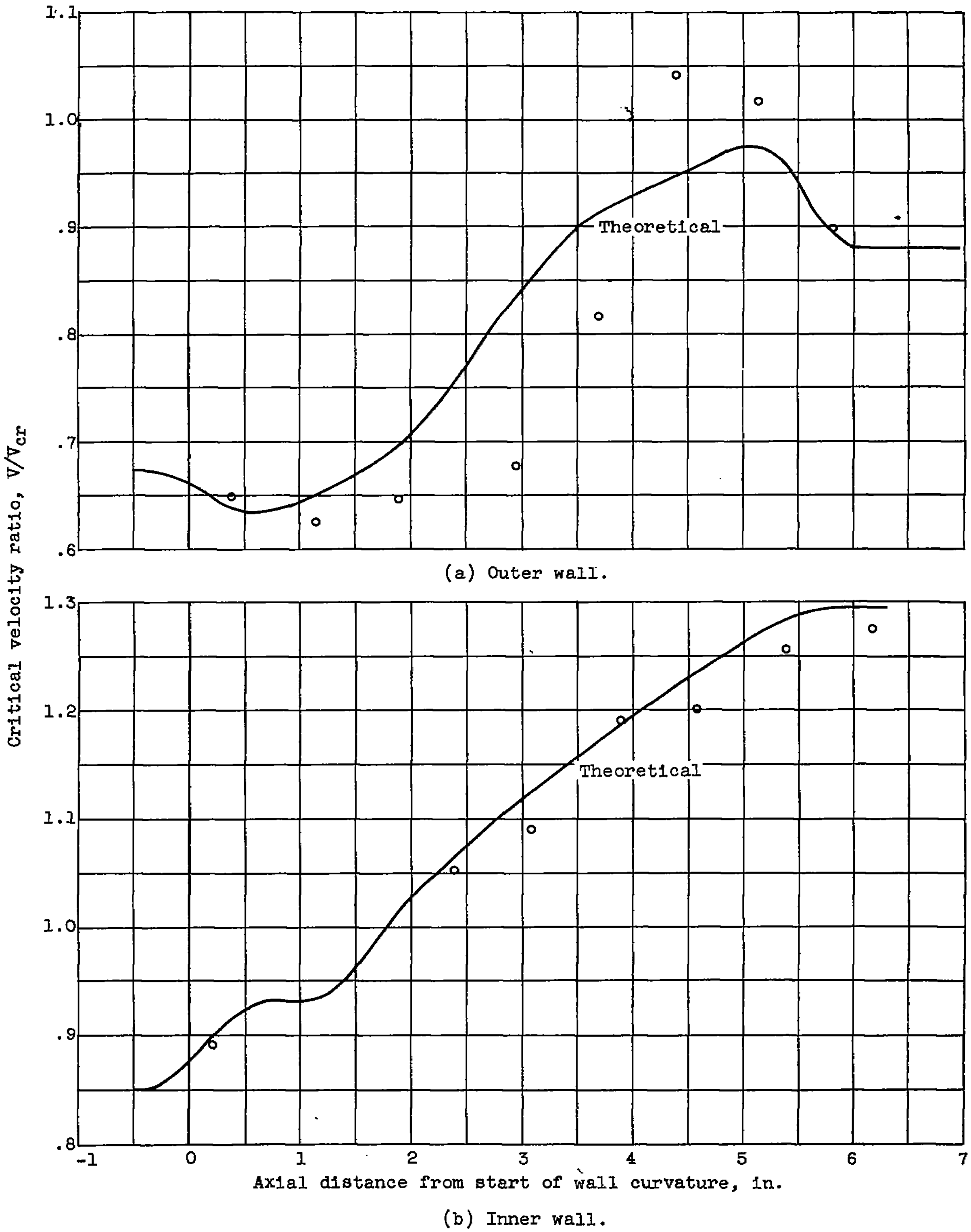

Figure 13. - Variation of critical velocity ratio at average exit critical velocity ratio of 1.056.

4356

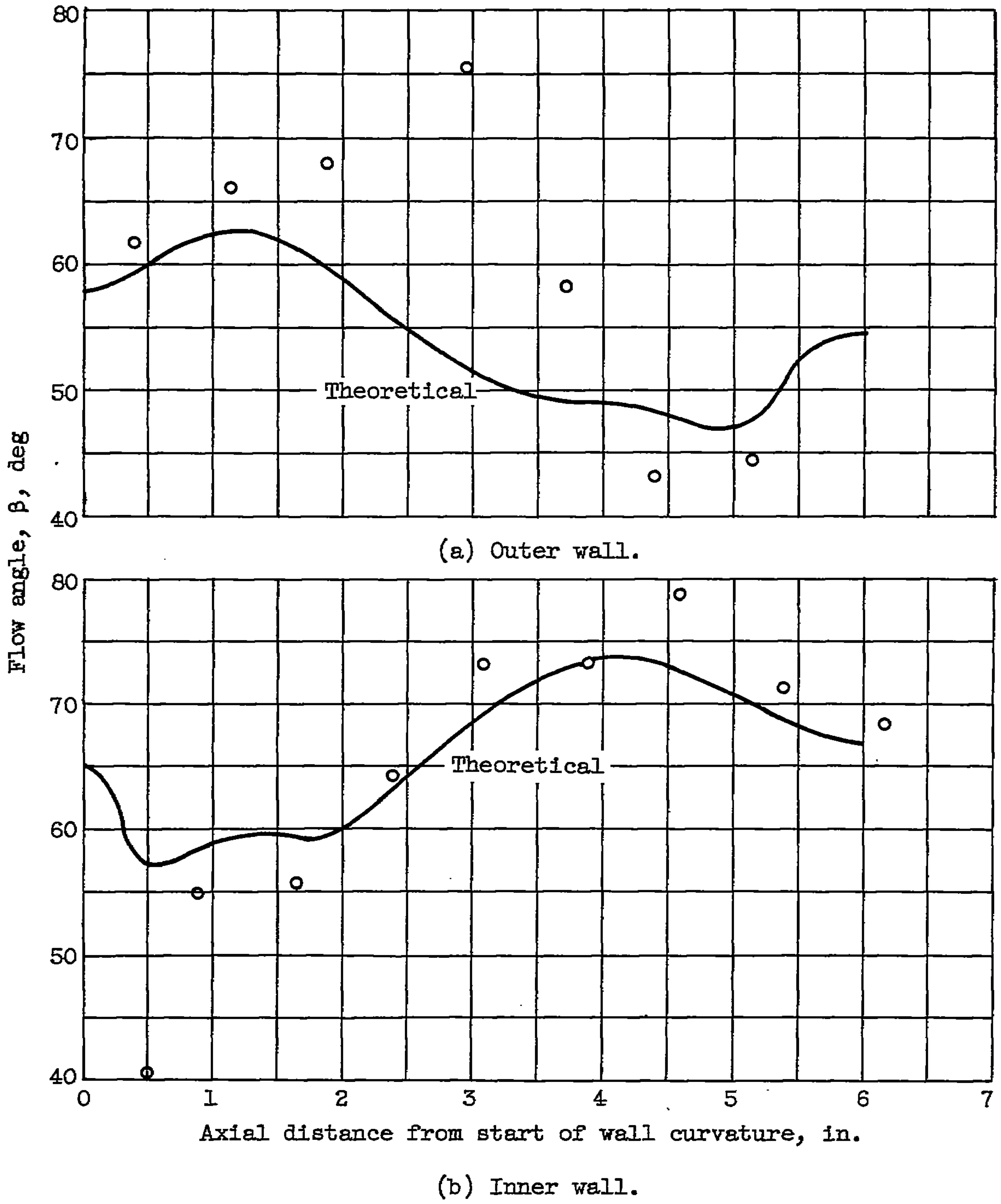

Figure 14. - Variation of flow angle on walls of vaneless transition section at exit average critical velocity ratio of 1.056.

4356

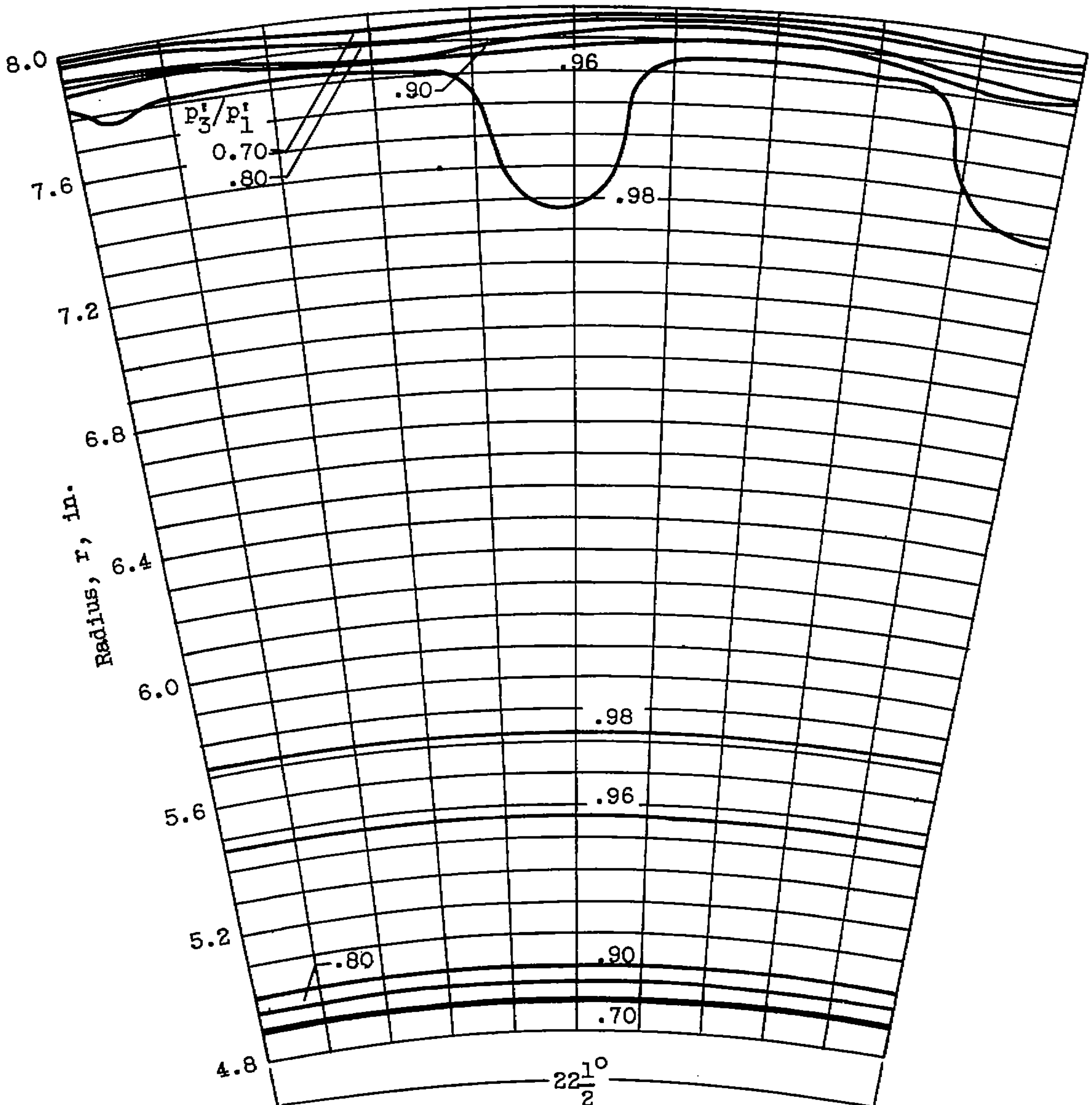

(a) Semivaneless stator.

Figure 15. - Contours of loss total-pressure ratio at stator exit.

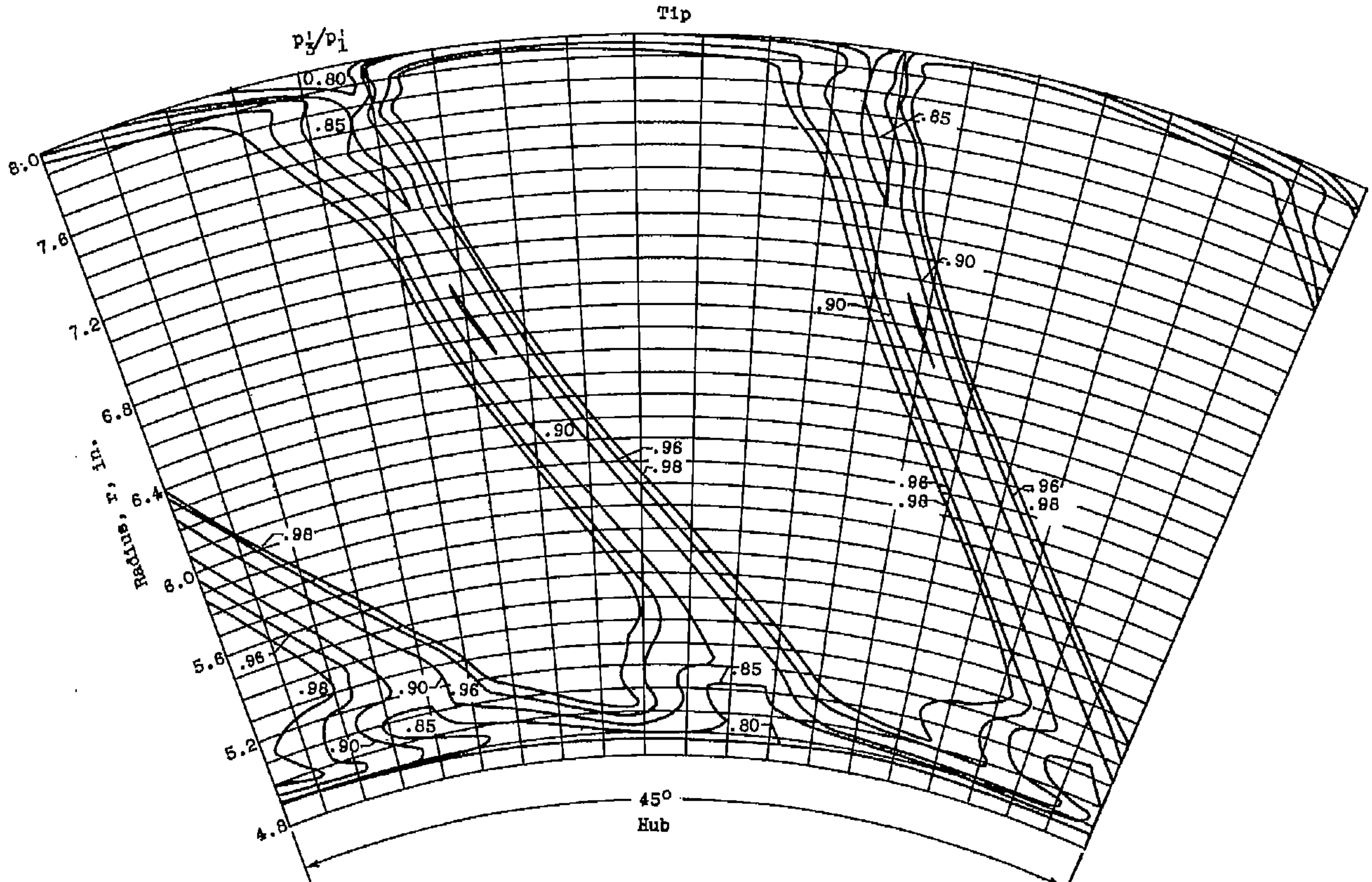

(b) Conventional stator.

Figure 15. - Concluded. Contours of loss total-pressure ratio at stator exit.

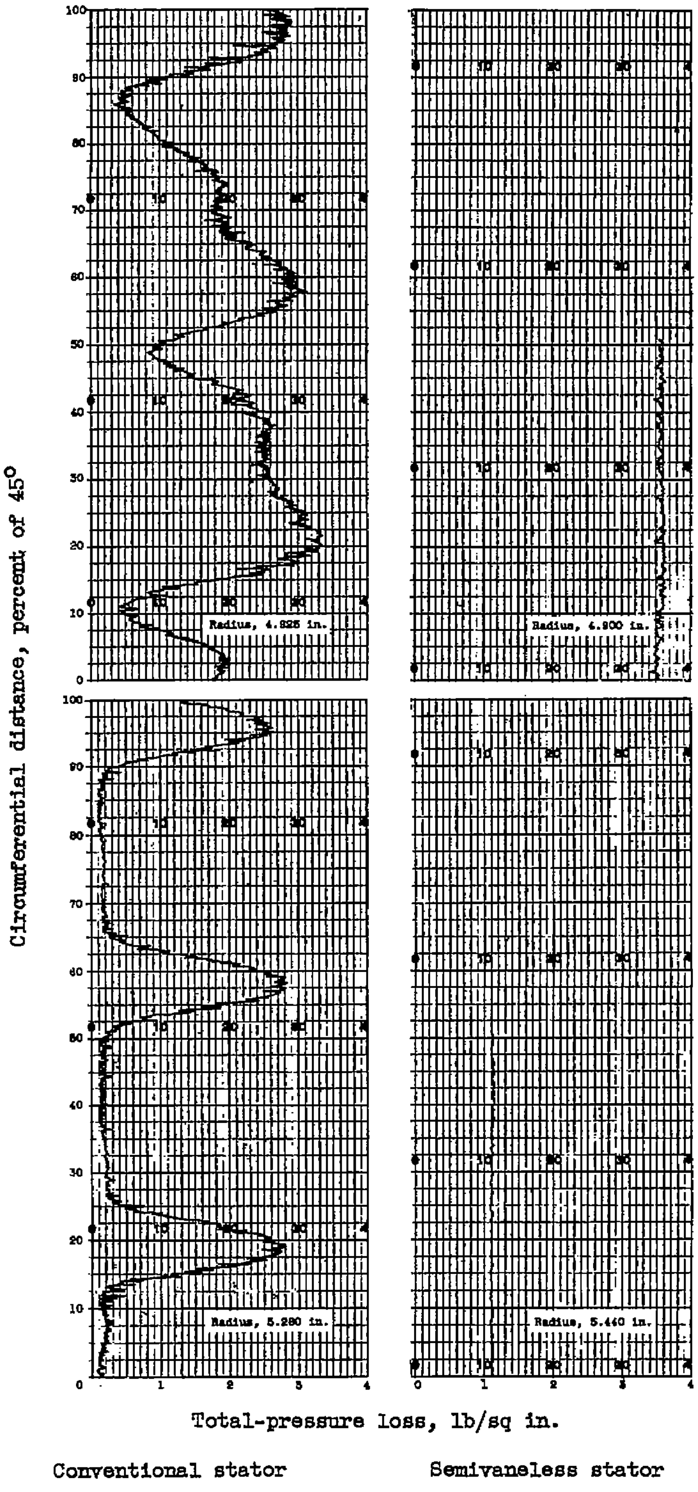

Figure 16. - Comparison of circumferential X-Y traces of total-pressure loss at exits of conventional and semivaneless stators with design stator-exit velocities.

4356

CL-5 back

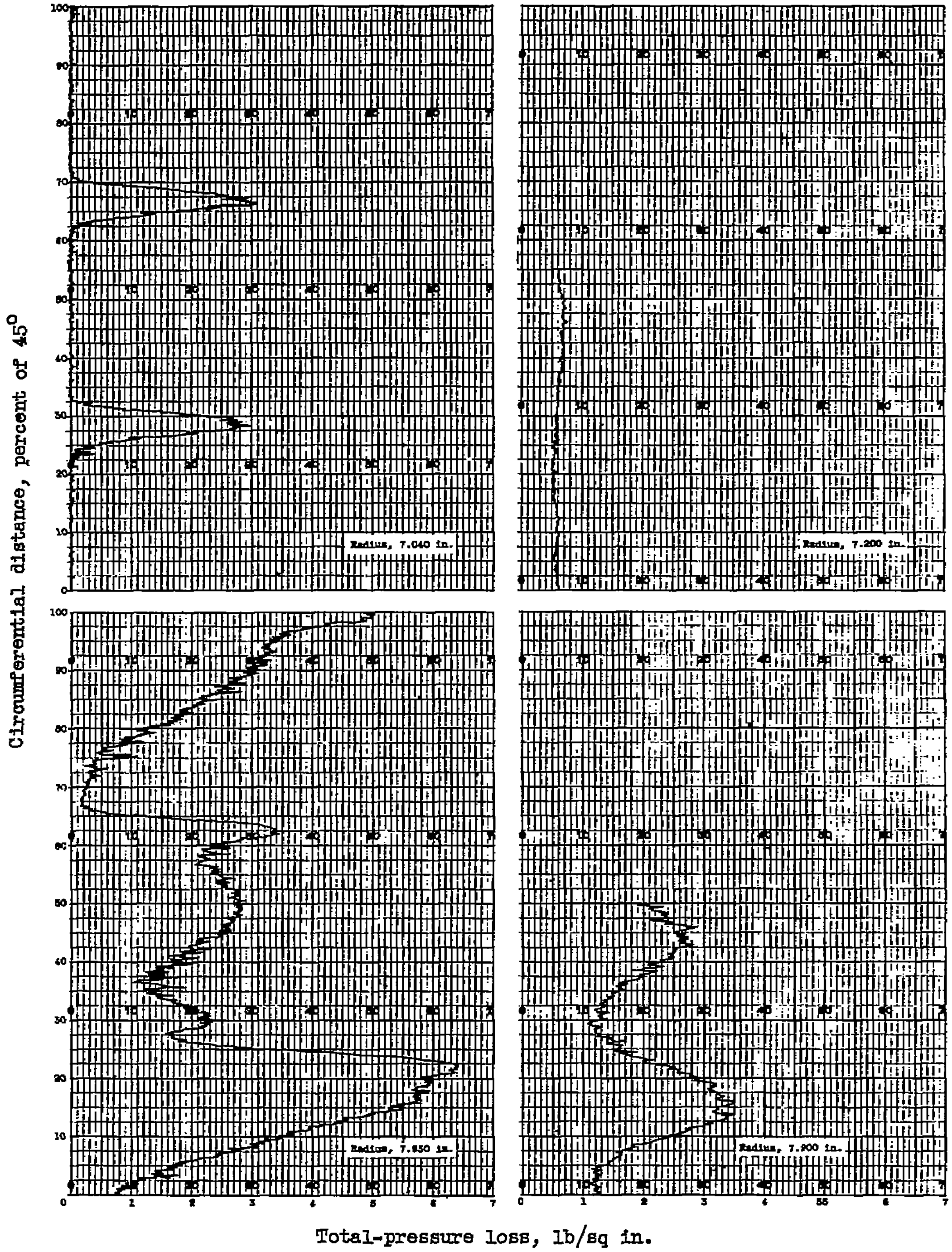

Conventional stator

Semivaneless stator

Figure 16. - Concluded. Comparison of circumferential X-Y traces of total-pressure loss at exits of conventional and semivaneless stators with design stator-exit velocities.

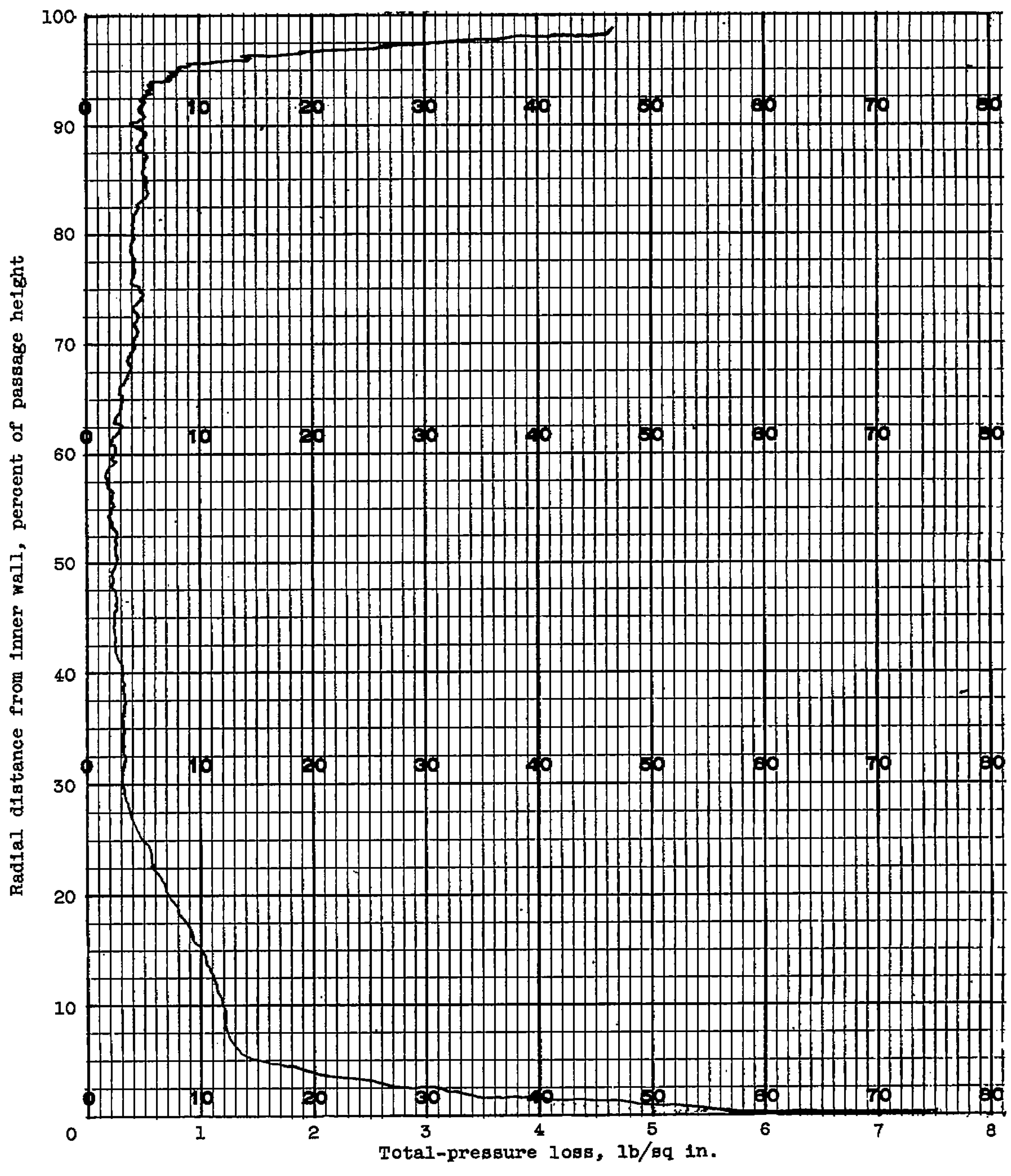

Figure 17. - Radial X-Y trace of total-pressure loss at exit of semivaneless stator with design stator-exit flow velocities.

4356

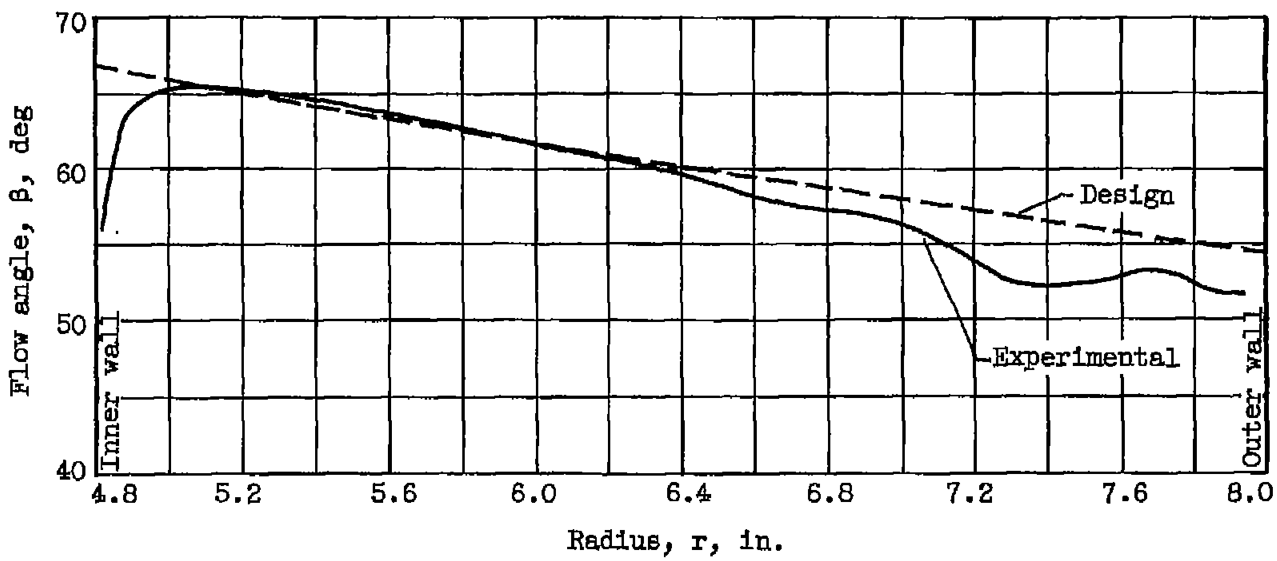

Figure 18. - Radial variation of flow angle at stator exit (station 3).

4356

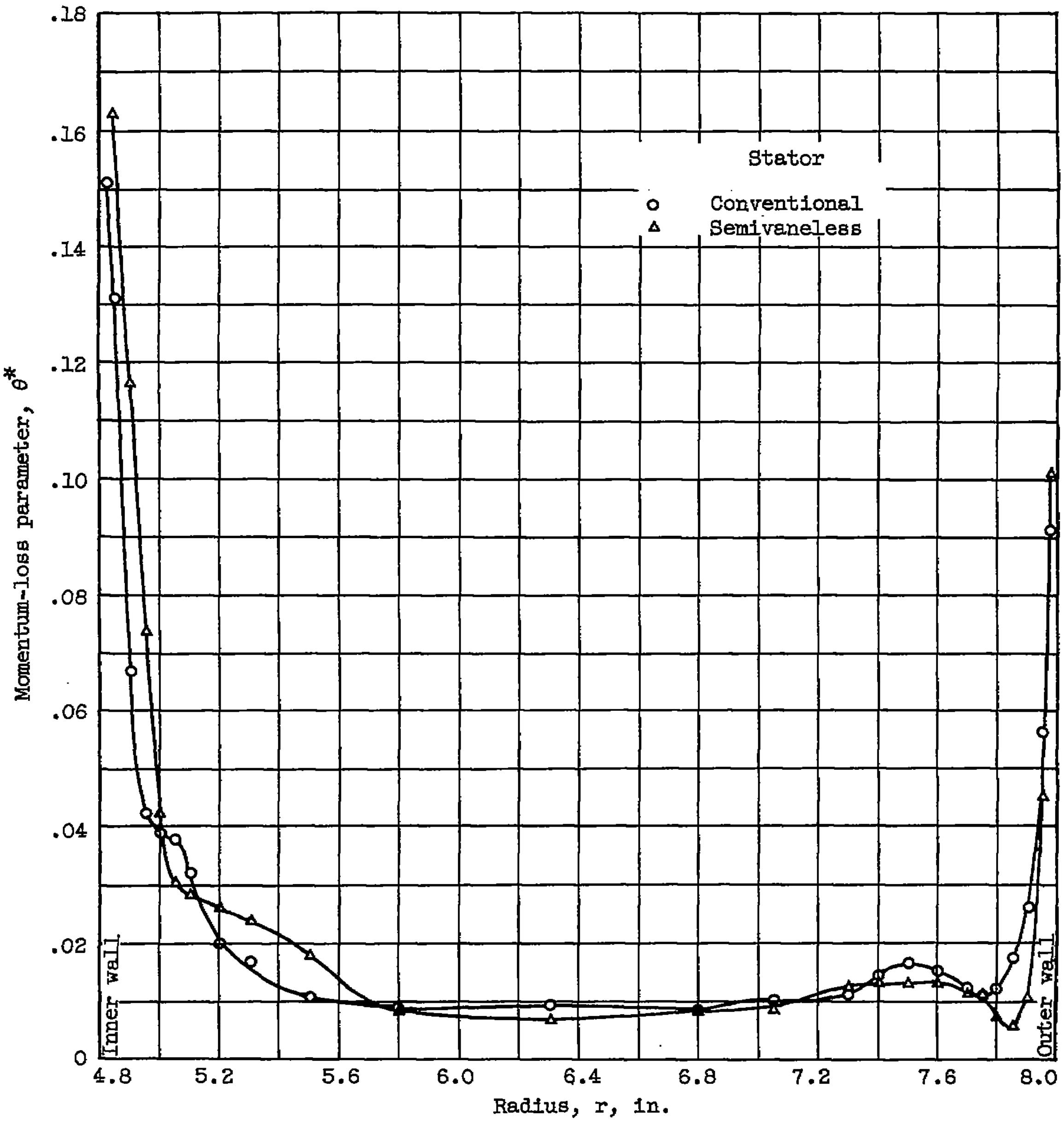

Figure 19. - Radial distribution of momentum-loss parameter at stator exit (station 3).

4356

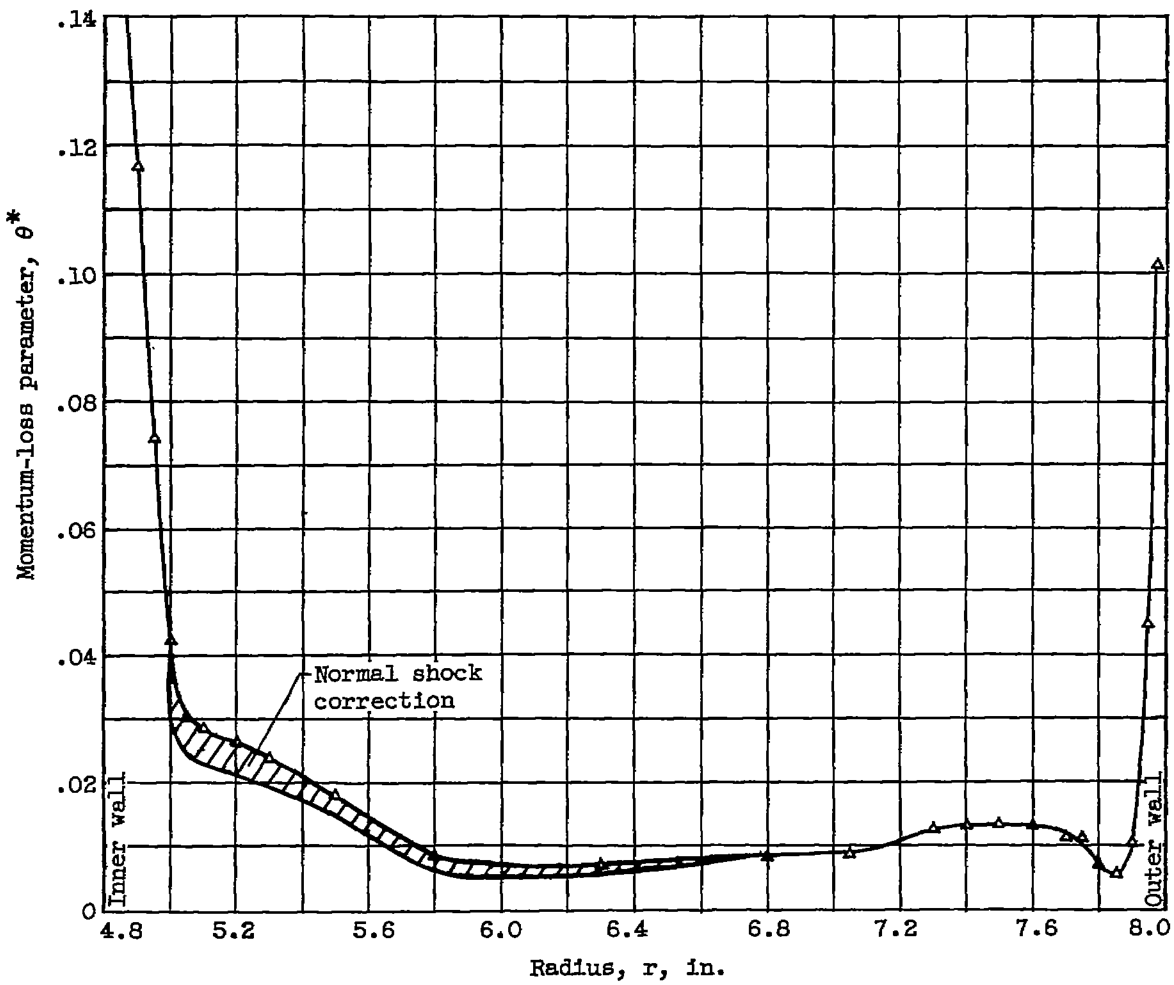

Figure 20. - Radial distribution of momentum-loss parameter of semi-vaneless stator at stator exit (station 3) showing normal shock correction.